

See discussions, stats, and author profiles for this publication at: <https://www.researchgate.net/publication/5337925>

Dynamics of Rhodobacter capsulatus [2Fe–2S] Ferredoxin VI and Aquifex aeolicus Ferredoxin 5 via Nuclear Resonance Vibrational Spectroscopy (NRVS) and Resonance Raman Spectroscopy †

ARTICLE *in* BIOCHEMISTRY · JUNE 2008

Impact Factor: 3.02 · DOI: 10.1021/bi701433m · Source: PubMed

CITATIONS

20

READS

64

12 AUTHORS, INCLUDING:



Hongxin Wang

University of California, Davis

77 PUBLICATIONS 1,187 CITATIONS

[SEE PROFILE](#)



Wolfgang Sturhahn

California Institute of Technology

330 PUBLICATIONS 5,331 CITATIONS

[SEE PROFILE](#)



Ercan E Alp

Argonne National Laboratory

394 PUBLICATIONS 5,310 CITATIONS

[SEE PROFILE](#)



Yoshitaka Yoda

Japan Synchrotron Radiation Research Ins...

193 PUBLICATIONS 2,391 CITATIONS

[SEE PROFILE](#)

Dynamics of *Rhodobacter capsulatus* [2Fe-2S] Ferredoxin VI and *Aquifex aeolicus* Ferredoxin 5 via Nuclear Resonance Vibrational Spectroscopy (NRVS) and Resonance Raman Spectroscopy[†]

Yuming Xiao,[‡] Ming-Liang Tan,^{||} Toshiko Ichiye,^{||} Hongxin Wang,[§] Yisong Guo,[‡] Matt C. Smith,[‡] Jacques Meyer,[⊥] Wolfgang Sturhahn,[#] Ercan E. Alp,[#] Jiyong Zhao,[#] Yoshitaka Yoda,[▽] and Stephen P. Cramer*,^{‡,§}

Department of Applied Science, University of California, Davis, California 95616, Physical Biosciences Division, Lawrence Berkeley National Laboratory, Berkeley, California 94720, Department of Chemistry, Georgetown University, Washington, D.C. 20057, Département Réponse et Dynamique Cellulaires (UMR 5090 CEA-CNRS-UJF), CEA-Grenoble, 38054 Grenoble, France, Advanced Photon Source, Argonne National Laboratory, Argonne, Illinois 60439, and JASRI, SPring-8, 1-1-1 Kouto, Sayo-cho, Sayo-gun, Hyogo 679-5198, Japan

Received July 20, 2007; Revised Manuscript Received March 18, 2008

ABSTRACT: We have used ⁵⁷Fe nuclear resonance vibrational spectroscopy (NRVS) to study the Fe₂S₂(Cys)₄ sites in oxidized and reduced [2Fe-2S] ferredoxins from *Rhodobacter capsulatus* (*Rc* FdVI) and *Aquifex aeolicus* (*Aa* Fd5). In the oxidized forms, nearly identical NRVS patterns are observed, with strong bands from Fe–S stretching modes peaking around 335 cm⁻¹, and additional features observed as high as the B_{2u} mode at ~421 cm⁻¹. Both forms of *Rc* FdVI have also been investigated by resonance Raman (RR) spectroscopy. There is good correspondence between NRVS and Raman frequencies, but because of different selection rules, intensities vary dramatically between the two kinds of spectra. For example, the B_{3u} mode at ~288 cm⁻¹, attributed to an asymmetric combination of the two FeS₄ breathing modes, is often the strongest resonance Raman feature. In contrast, it is nearly invisible in the NRVS, as there is almost no Fe motion in such FeS₄ breathing. NRVS and RR analysis of isotope shifts with ³⁶S-substituted into bridging S²⁻ ions in *Rc* FdVI allowed quantitation of S²⁻ motion in different normal modes. We observed the symmetric Fe–Fe stretching mode at ~190 cm⁻¹ in both NRVS and RR spectra. At still lower energies, the NRVS presents a complex envelope of bending, torsion, and protein modes, with a maximum at 78 cm⁻¹. The ⁵⁷Fe partial vibrational densities of states (PVDOS) were interpreted by normal-mode analysis with optimization of Urey–Bradley force fields. Progressively more complex D_{2h} Fe₂S₂S'₄, C_{2h} Fe₂S₂(SCC)₄, and C₁ Fe₂S₂(Cys)₄ models were optimized by comparison with the experimental spectra. After modification of the CHARMM22 all-atom force field by the addition of refined Fe–S force constants, a simulation employing the complete protein structure was used to reproduce the PVDOS, with better results in the low frequency protein mode region. This process was then repeated for analysis of data on the reduced FdVI. Finally, the degree of collectivity was used to quantitate the delocalization of the dynamic properties of the redox-active Fe site. The NRVS technique demonstrates great promise for the observation and quantitative interpretation of the dynamical properties of Fe–S proteins.

Plant- and mammalian-type [2Fe-2S] ferredoxins are generally small (~90–130 amino acid residues) electron-transfer proteins with a single Fe₂S₂(S-cys)₄ redox center (*1–3*). On the basis of their functional roles and structures, most of these proteins can be distributed into three main subgroups, namely, plant-type, mammalian-, vertebrate-, or

hydroxylase-type, and Isc-type ferredoxins. In the first subgroup, in plants and algae, [2Fe-2S] ferredoxins mediate electron transfer between photosystem I and enzymes involved in NADPH production, sulfur and nitrogen assimilation, and nitrogen fixation (*3*). A better understanding of this process could have important biotechnological applications since electron transfer between ferredoxin and NADP via FNR has been shown to be the rate-limiting step in photosynthesis (*4*). In the second subgroup, [2Fe-2S] ferredoxins are involved in electron transfer to hydroxylases and oxygenases, in vertebrates, and also over a wide range of organisms including bacteria. Ferredoxins in the third subgroup play a role in Fe–S cluster biosynthesis (*5*). As more sequence information has emerged, the relationships between [2Fe-2S] ferredoxins have been illuminated by dendograms based on sequence similarity (Chart 1) (*6*). It should be noted that the second and third subgroups are overlapping, as some Isc-type Fds appear, on the basis of

* To Whom correspondence should be addressed. Tel: (530) 752-0360. Fax: (530) 752-2444. E-mail: spjcramer@ucdavis.edu.
[†] This work was funded by NIH Grants GM-65440 (to S.P.C.), EB-001962 (to S.P.C.), and GM-45303 (to T.I.), and the DOE Office of Biological and Environmental Research (to S.P.C.). Use of the APS is supported by the DOE Office of Basic Energy Sciences, Office of Science. SPring-8 is funded by JASRI.

[‡] University of California-Davis.
[§] Lawrence Berkeley National Laboratory.

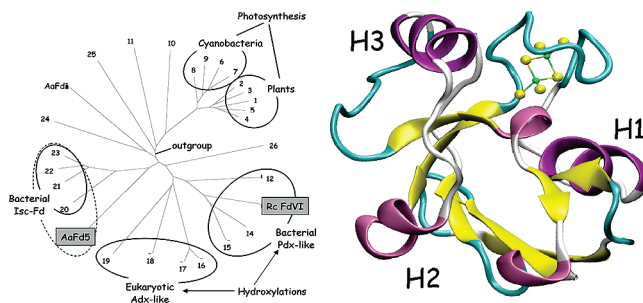
^{||} Georgetown University.

[⊥] CEA-Grenoble.

[#] Argonne National Laboratory.

[▽] SPring-8.

Chart 1: Dendrogram Based on Sequence Similarity between Different [2Fe-2S] Ferredoxins (Left) and VMD (10) Ribbon Representation for Oxidized *Rc* FdVI, Including [2Fe-2S] Cluster (Right)



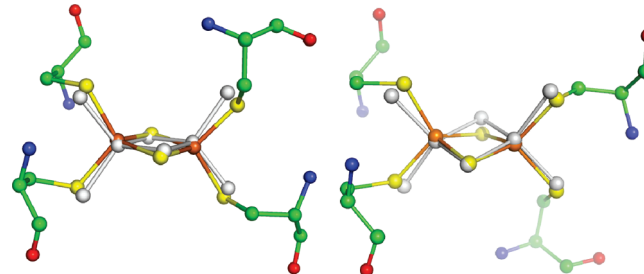
sequence similarity alone, to belong to the hydroxylation-type subgroup.

Rhodobacter capsulatus is a photosynthetic bacterium (α -Proteobacteria) with 6 distinct ferredoxin-encoding genes (7), all of which have been characterized genetically/biochemically in the Jouanneau group (7, 8). Comparative genomics suggests that the sixth ferredoxin from this organism, *Rc* FdVI, is involved in the synthesis of iron–sulfur clusters (8), despite its seemingly closer overall sequence similarity to hydroxylation-type ferredoxins (see dendrogram in Chart 1). X-ray crystal structures for *Rc* FdVI, in the oxidized (2.07 Å resolution - 1E9M) and reduced forms (2.00 Å resolution - 1UWM) have recently been determined and compared (8). The structures for both forms (8) have been described as the same $\alpha\beta$ fold observed for other [2Fe-2S] ferredoxins (1–3), a twisted β -sheet composed of 5 β -strands, flanked by one major α -helix (H1 in Chart 1). Two minor helices (H2 and H3 in Chart 1) are present in a large hairpin referred to as the interaction domain. The [2Fe-2S] cluster lies 5–6 Å from the surface within a loop in the so-called core domain. *Rc* FdVI shares the Cys-X₃-Cys-X₁-Cys-X₂-Cys cluster-binding motif of other Fds known to be involved in Fe–S cluster biosynthesis (8), where the second cysteine, which is not a cluster ligand, has been proposed as a binding site for Fe or S (9). *Rc* FdVI shows strong sequence homology with Pdx (8), and in the crystal structures, an overall rms deviation of only 1 Å was determined between main-chain C_α atoms of *Rc* FdVI and Pdx (8).

The oxidized *Rc* FdVI structure reveals a planar [Fe₂S₂] core and approximate D_{2h} symmetry for the Fe₂S^b₂S^t₄ portion of the Fe₂S₂Cys₄ site (Chart 2). The orientations of the cysteine side chain carbons break this site symmetry. Conversion from oxidized to reduced forms results in a slight puckering of the Fe₂S₂ core, as well as conformational changes at neighboring Met24 and Ala44 residues. The side chain of Met24 rotates 180°, bringing the thioether S within 2.85 Å of the cluster bridging S2. In addition, the Ala44 carbonyl O changes from pointing away from the cluster (“CO out” conformation) to pointing toward the cluster (“CO in” conformation). This conformational change brings it within 3.0 Å of the Met70 S and 3.9 Å of the cluster bridging S1.

Conformational changes have been observed upon reduction of other [2Fe-2S] ferredoxins, including the plant-type [2Fe-2S] *Anabaena* PCC7119 ferredoxin (Fd7119) (12), the vertebrate type adrenodoxin (Adx) (13, 14), and the vertebrate-type putidaredoxin (Pdx) (15). In Fd7119, which also exhibits

Chart 2: Oxidized *Rc* FdVI 2Fe-2S Site (Color) Using Crystal Structure Coordinates (1E9M) Compared to a Hypothetical Fe₂S₂S^t₄ Model with D_{2h} Symmetry (Gray) (Left) and Reduced *Rc* FdVI 2Fe-2S Site (Color) Using Crystal Structure Coordinates (1UWM) vs a Hypothetical Fe₂S₂S^t₄ Model with D_{2h} symmetry (Gray) (Right)^a



^a Figures made with Pymol (11), and H atoms omitted for clarity.

a “CO out–CO in” isomerization for its Cys46 carbonyl group (12), molecular mechanics calculations find that the “CO in” form will rapidly convert to the “CO out” form upon reduction (16). With Adx, it was proposed that the switch for detachment from adrenodoxin reductase (AdR) is the redox state of the [2Fe-2S] cluster (17), and molecular dynamics studies suggest that redox-induced changes in the flexibility of a 5 residue loop surrounding the iron–sulfur cluster could affect the binding and dissociation of Adx from AdR (17). In a similar vein, the reduced form of Pdx has a binding constant for cytochrome P-450_{cam} that is 2 orders of magnitude higher than that of the oxidized Pdx (18). This is a catalytically important effect that helps prevent product inhibition in the electron transfer reaction between P-450 and Pdx (19). On the basis of paramagnetic effects on NMR spectra, residues Gly40 and Gly41 in the Pdx metal binding loop were proposed as potential hinges for conformational fluctuations (20), and additional evidence for this hypothesis came from Gly40 → N site-directed mutagenesis (19).

For a variety of related [2Fe-2S] Fds, the frequencies of stretching modes are available from resonance Raman spectroscopy. In the oxidized forms, the Raman spectra generally exhibit 6 or 7 resolved peaks between 280 and 430 cm⁻¹ (6, 21–23), which correspond to 8 Fe–S stretching modes (2 of which are unresolved) in D_{2h} symmetry for a Fe₂S^b₂S^t₄ core (24). Spiro and co-workers used a Urey–Bradley force field with an Fe₂S^b₂(S'CC)₄ model to successfully reproduce most of the Fe–S stretching frequencies. As with rubredoxin (25–27), they emphasized the importance of Fe–S–C–C dihedral angles for coupling Fe–S stretching with S–C–C bending (24) and proposed that the Fe–S^t stretching mode frequencies can be used as diagnostics for the local conformation. In some cases, the predictions have been quite successful, while in other cases the correlation is less apparent (Table S1). For example, Han and co-workers predicted dihedral angles of 105° for *S. platensis* ferredoxin (22), and the most recent crystal structure (PDB entry 4FXC) reveals values of 120, 123, 100, and 100° (28). For comparison, Fu and co-workers used the 319 cm⁻¹ frequency of the “B₂ Fe–S” stretching mode in putidaredoxin to predict dihedral Fe(III)–S–C_β–C_α angles close to 90° or 270° for the cysteines ligated to the Fe(III) site (21). However, in the reduced Pdx structures that have recently become available (albeit for mutant proteins), the Fe(III)-S- C_β-C_α dihedral

angles are at an average of 124° (29). Similarly, the increased separation between the B_{3u}^t mode and A_g^t , B_{2g}^t , and B_{3u}^b modes has been used to argue for more planar Fe(III)-S-C β -C α dihedral angles in *T. vaginalis* ferredoxin compared to Pdx (30). Yet, the subsequent crystal structure of *T. vaginalis* ferredoxin (PDB entry 1L5P) revealed Fe(III)-S-C β -C α dihedral angles at an average of 113° (31), compared to the 120° average found in Pdx (29).

Rotsaert et al. observed ^{15}N isotope shifts for modes at 282, 340, and 357 cm $^{-1}$ in the resonance Raman of *Anabaena* Fd, indicating coupling of C β -C α -N deformation to Fe-S stretching (32). Furthermore, since the Fe-S-C β -C α dihedral angles in this protein are between 90° and 120° (33), they concluded that “some kinematic coupling is feasible among bonded atoms that are not coplanar” (32). The degree of coupling between Fe-S stretching and deformations of the polypeptide backbone has also been debated for [2Fe-2S] Rieske proteins (34).

For [2Fe-2S] model compounds (24), other Raman bands have been seen below 200 cm $^{-1}$, and these features have been assigned as a mixture of Fe-S-C and S-Fe-S bending modes. However, since only a few modes of those expected for even the simplest Fe₂S^b₂(S'CC)₄ model are observed in Raman spectra, the bend and torsion components of Fe-S cluster empirical force fields are generally not well defined. The lower frequency cluster modes may exhibit stronger coupling to protein deformation modes.

The dynamical characteristics of the oxidized and reduced metal sites play an important role in the properties of Fe-S clusters and their associated proteins. Redox-dependent changes in metalloprotein structure have been known for several decades (35, 36). Apart from their significance with [2Fe-2S] Fds and their partners (17–19), such conformational changes seem to play a role in electron transfer in photosynthesis (37), in the binding and release of the nitrogenase Fe protein to its MoFe protein partner (38), and in the many complex events requiring Fe-S proteins (39) including nitrogenase (40) and hydrogenase (41). Considering the number of predictions that have been made and the lingering issues about the normal mode compositions, it is clear that more information about [2Fe-2S] cluster dynamics would be useful for any predictions about structure and function in Fe-S proteins. To obtain such information, we have examined *Rc* FdVI by a combination of resonance Raman spectroscopy and nuclear resonance vibrational spectroscopy (NRVS), interpreted by normal mode calculations with a modified CHARMM force field.

NRVS is rapidly becoming a popular technique for probing the dynamics of Fe in metalloproteins (42, 43). This measurement involves scanning an extremely monochromatic X-ray beam through a nuclear resonance. Apart from the zero phonon recoil-free Mössbauer resonance, there are transitions that correspond to nuclear excitation plus creation (Stokes) or annihilation (anti-Stokes) of phonons. The NRVS intensity for a given normal mode is proportional to the motion of the resonant nucleus j (in this case ^{57}Fe) along the direction of the incident X-ray beam (43, 44). For a randomly oriented sample, a NRVS transition for normal mode α contributes a fraction φ_α to the normalized excitation probability $S(\bar{\nu})$ that is directly proportional to the Fe mode composition factor $e_{j\alpha}^2$ and inversely proportional to $\bar{\nu}_\alpha$ (44, 45):

$$\varphi_\alpha = \frac{1}{3} \frac{\bar{\nu}_R}{\bar{\nu}_\alpha} e_{j\alpha}^2 (\bar{n}_\alpha + 1) f \quad (1)$$

In the above equation, $\bar{\nu}_\alpha$ is the difference between the photon energy and the recoil-free nuclear resonance energy in wave numbers, $\bar{\nu}_R$ is the recoil energy ($\sim 16 \text{ cm}^{-1}$), $\bar{n}_\alpha = [\exp(hc\bar{\nu}_\alpha/k_B T) - 1]^{-1}$ is the thermal occupation factor for a mode of frequency $\bar{\nu}_\alpha$ at temperature T (44), and the recoilless fraction f depends on $\langle x_{\text{Fe}}^2 \rangle$, the mean square fluctuation of the Fe nucleus along the beam direction, via $f = \exp(-k^2 \langle x_{\text{Fe}}^2 \rangle)$. It is also useful to define an ^{57}Fe -centered partial vibrational density of states (PV DOS), $D_{Fe}(\bar{\nu})$, using a line shape function $\mathcal{L}(\bar{\nu} - \bar{\nu}_\alpha)$ (44, 46):

$$D_{Fe}(\bar{\nu}) = \sum_\alpha e_{Fe,\alpha}^2 \mathcal{L}(\bar{\nu} - \bar{\nu}_\alpha) \quad (2)$$

The ^{57}Fe PV DOS can be extracted from the raw NRVS using the PHOENIX software package (47), and the Fe mode composition factor $e_{Fe,\alpha}^2$ for a given eigenvector can be calculated from a normal-mode analysis via (44, 48):

$$e_{Fe,\alpha}^2 = \frac{m_{Fe} r_{Fe,\alpha}^2}{\sum_i m_i r_{i\alpha}^2} \quad (3)$$

where m_i and $r_{i\alpha}^2$ are the mass of atom i and its mean square motion in mode α , respectively.

In this article, we report the ^{57}Fe NRVS for oxidized and reduced forms of ^{57}Fe -enriched *Rc* FdVI, both with natural abundance sulfur as well as with ^{36}S in the bridging sulfide positions. NRVS data for ^{57}Fe -enriched oxidized and reduced forms of another [2Fe-2S] ferredoxin, *Aquifex aeolicus* Fd5, are included for comparison. Resonance Raman spectra for all of the *Rc* FdVI and *Aa* Fd5 samples are also presented. Normal mode calculations on models of increasing complexity are used to reproduce and interpret the experimental data. By combining NRVS and Raman spectra, we were able to refine Urey-Bradley force fields for both oxidized and 1-electron reduced sites. The NRVS data also reveal low frequency modes not evident in the Raman spectra. The results are compared with previous Raman and molecular mechanics analyses of [2Fe-2S] ferredoxins.

EXPERIMENTAL PROCEDURES

Protein Purification and Sample Preparation. *Aquifex aeolicus* Fd5 (*Aa* Fd5) was produced in *Escherichia coli* and purified as described (6), but with ^{57}Fe in the growth medium. For that purpose, metallic ^{57}Fe was dissolved in a mixture of concentrated HCl and HNO₃ and added to the medium for a final concentration of 1 mg/L. *Rhodobacter capsulatus* FdVI (*Rc* FdVI) was produced in *E. coli* as described (7), but the medium was as indicated above for *Aa* Fd5. *Rc* FdVI was purified as described above for *Aa* Fd5, except that the heat treatment was omitted. With these procedures, both *Aa* Fd5 and *Rc* FdVI were obtained directly as ^{57}Fe -enriched proteins. The A415/A276 absorption ratios of purified *Aa* Fd5 and *Rc* FdVI were 0.70 and 0.54, respectively.

The preparation of ^{36}S -enriched *Rc* FdVI was performed as described for ^{34}S -substitution in spinach ferredoxin (49). A critical step was the implementation of HCl (0.5 N) and anaerobic conditions for denaturation of the holoprotein. For the reconstitution, elemental ^{36}S was reduced to the S $^{2-}$

oxidation level by heating in a dihydrogen atmosphere, and ^{57}Fe was implemented in the reconstitution reaction. The UV-visible absorption spectrum of the reconstituted Fd was identical to the spectrum of the native protein, except for a slightly lower A414/A278 ratio (0.50 versus 0.54). A reduced sample was prepared by dithionite reduction in an anaerobic N_2 -containing glovebox. Both of the ^{36}S -enriched *Rc* FdVI samples have ^{36}S in the [2Fe-2S] cluster bridging positions, and natural abundance sulfur in the cysteine thiolates.

Nuclear Resonance Vibrational Spectroscopy. ^{57}Fe NRVS spectra were recorded using published procedures (43) on multiple occasions at Beamline 3-ID at the Advanced Photon Source (APS) (50) and Beamline 9-XU at SPring-8, Japan (51). Beamline 3-ID provided $\sim 2.5 \times 10^9$ photons/s in 1 meV bandwidth at 14.4125 keV in a 1 mm (vertical) \times 3 mm (horizontal) spot, using a water-cooled diamond (1,1,1) double crystal monochromator with 1.1 eV bandpass, followed by separate Si(4,0,0) and Si(10,6,4) channel-cut crystals in a symmetric geometry. The flux at SPring-8 was $\sim 3 \times 10^9$ in a 1.1 meV bandwidth, using a LN₂-cooled Si(1,1,1) double crystal monochromator followed by asymmetrically cut Ge(4,2,2) and two Si(9,7,5) crystals. For NRVS measurements, protein samples were loaded into 3 \times 7 \times 1 mm³ (interior dimensions) Lucite cuvettes. During these measurements, samples were maintained at low temperatures using liquid He cryostats. Temperatures were calculated using the ratio of anti-Stokes to Stokes intensity according to: $S(-E) = S(E)\exp(-E/kT)$. Spectra were recorded between -20 and 80 meV in 0.25 meV steps at APS and 0.3 meV steps at SPring-8. Nuclear fluorescence and Fe K fluorescence (from internal conversion) were recorded with a single 1 cm² square avalanche photodiode (APD) at the APS and with an APD array at SPring-8. Each scan took about 40 min, and all scans were added and normalized to the intensity of the incident beam.

Raman Spectroscopy. Resonance Raman spectra were recorded in backscattering geometry from drops of *Rc* FdVI and *Aa* Fd5 solutions frozen on a Au-plated Cu coldfinger inside an Oxford Optistat-DN LN₂ cryostat at 77 K. The excitation source was a Coherent Innova-2 Ar⁺/Kr⁺ laser, using a power of ~ 35 mW. No sample radiation damage was observed. The spectra were recorded at ~ 6 cm⁻¹ resolution with a Spex model 1877 triple spectrograph, using a cooled Spectrum One 594 CCD detector. Each spectrum represents ~ 8 –16 h of measurement. The spectra were calibrated versus 218 cm⁻¹ and 314 cm⁻¹ peaks in a room temperature CCl₄ sample.

Normal Mode Calculations. The crystal structures for oxidized and reduced *Rc* FdVI (1E9M and 1UWM, respectively) were used as starting points (8), and symmetrized models were derived from these coordinates using the program Atoms (52, 53). The local site normal mode calculations were carried out with a Urey–Bradley force field using a modification of the program Vibratz (52, 53). A QR algorithm was used for finding eigenvectors (54). The resulting normal modes were broadened by a convolution with a 10 cm⁻¹ fwhm Voigt profile. The parameters of the force field were optimized by minimizing the residual Δ defined by:

$$\Delta = \frac{1}{N} \sum_i^N (D_{\text{obs}}(\nu_i) - D_{\text{calc}}(\nu_i))^2 + \frac{c}{M} \sum_j^M (\nu_j^{\text{obs}} - \nu_j^{\text{calc}})^2 \quad (4)$$

In the above equation, $D_{\text{obs}}(\nu_i)$ and $D_{\text{calc}}(\nu_i)$ are, respectively, the observed and calculated ^{57}Fe PVOS at frequency ν_i , N is the number of NRVS data points, ν_j^{obs} and ν_j^{calc} are, respectively, the observed and calculated Raman frequencies, M is the number of observed Raman frequencies, and c is a weighting factor to adjust the relative importance of NRVS and Raman data sets. Initially, the weighting factor used was 1000. This essentially forced the optimization to match the Raman frequencies as well as possible, and within that constraint, to reproduce the NRVS. Subsequently, we found that if the PVDOS were in units of eV⁻¹ and the Raman frequencies were in units of cm⁻¹, then a weighting factor of ~ 1 yielded better fits to the NRVS data, while still matching the Raman constraints reasonably well.

For the full protein calculations, H atom positions were built using the HBUILD facility of CHARMM 33 (55). The systems contain 1586 protein atoms and 56 crystal water molecules (142 waters for reduced protein). The force field parameters consisted of the CHARMM22 all-atom parameters (55) plus additional parameters for the Fe₂S₆ assembly as initially obtained from the local site optimization. To obtain a structure for the full protein normal mode calculation, it was necessary to refine the crystal structures (1E9 M and 1UWM) to a minimal energy conformation. Constraints were introduced during the minimizations that led to a minimal energy structure close to the crystal structure, and a mass-weighted atomic harmonic potential was applied to each heavy atom. The systems were energy-minimized by 1000 steps of steepest descent method followed by successive sets of Adopted Basis Newton–Raphson (ABNR) minimizations (500 steps each) with the constraints reduced and the reference structure updated for each set; the final constraint constant was 0.05 kcal/mol/Å² per atomic mass. The normal mode calculations were then performed without constraints using the VIBRAN module in the CHARMM 33 program (55). For comparison with the experimental spectra, Gaussian functions were calculated centered around each ω_α , the frequency of mode α , using an 8 cm⁻¹ fwhm and amplitude proportional to $e_{j\alpha}^2$. The ^{57}Fe PVDOS was then obtained by summing these Gaussian functions over all modes.

Degree of Collectivity Calculations. The degree of collectivity κ for normal mode α , first proposed by Bruschweiler (56), was calculated by the equation given by Tama and Sanejouand (57), except that the cluster Fe and S atoms were included in the summation along with all non-hydrogen protein atoms:

$$\kappa = \frac{1}{N} \exp\left(-\sum_i^N a r_{i\alpha}^2 \log ar_{i\alpha}^2\right) \quad (5)$$

where a is a normalization factor chosen so that $\sum_i^N a r_{i\alpha}^2 = 1$.

RESULTS AND DISCUSSION

Resonance Raman Spectra. We discuss the resonance Raman data first, since there is a wealth of similar spectra available for other [2Fe-2S] ferredoxins, including spinach (21, 58), *Anabaena*, and *Porphyra umbilicalis* Fds (32), bovine (22) and human (23) Adxs, *Aa* Fd1 (23) and Fd5 (6), Pdx (21), and [2Fe-2S] sites in hydrogenases (59). When excited at 514.5 nm, the spectrum for *Rc* FdVI exhibits

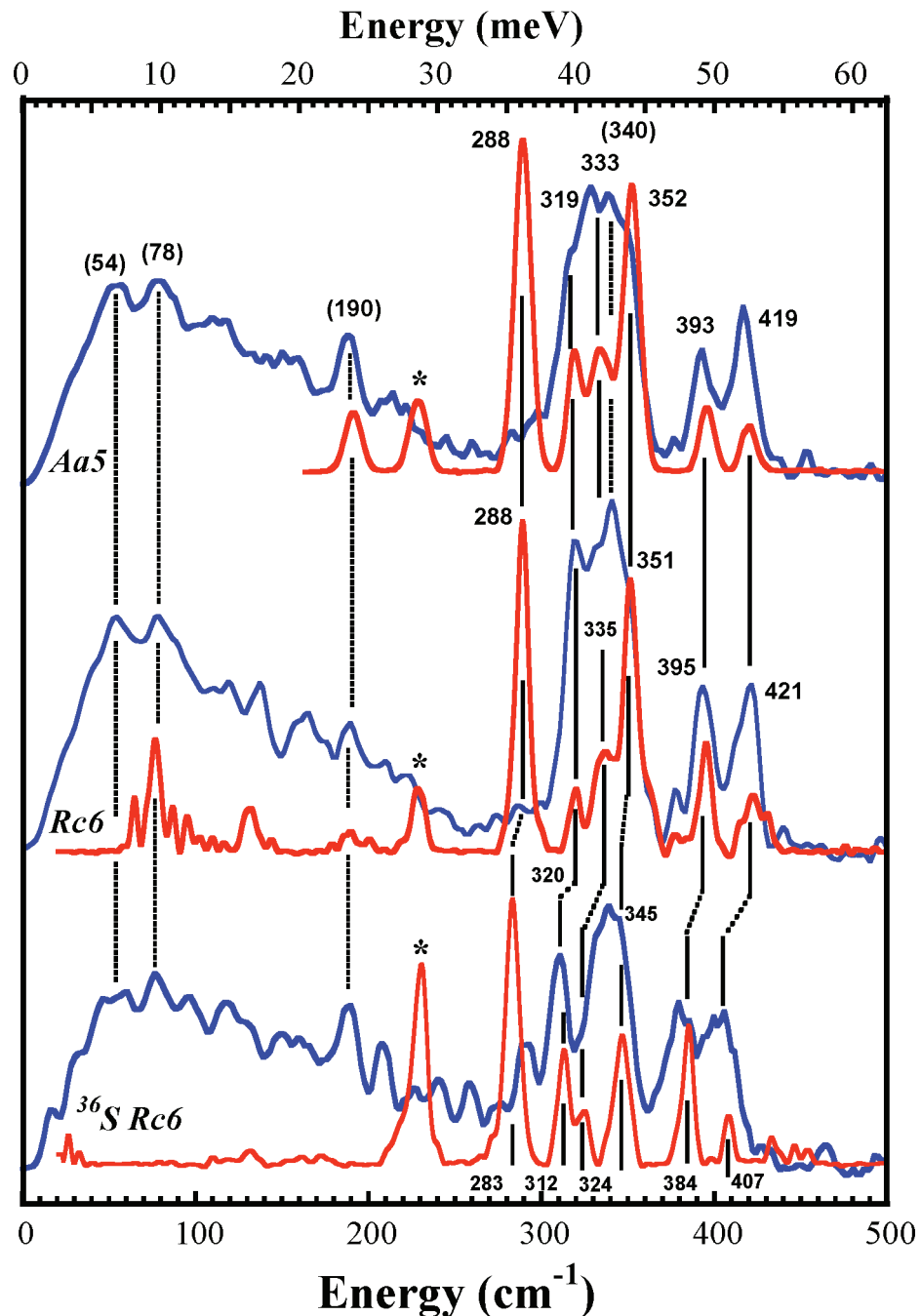


FIGURE 1: Top to bottom: resonance Raman spectra, using excitation at 515 nm (red line), compared with ^{57}Fe PVDOS (blue line) for oxidized, ^{57}Fe -enriched (a) *AaFd5*, (b) *RcFdVI*, and (c) ^{36}S -substituted *Rc FdVI*. * Marks ice band in Raman spectra. Dashed vertical lines highlight common PVDOS features between spectra; solid lines mark Raman peak positions. Numbers in parentheses refer to PVDOS peaks; the remaining values are Raman peak positions.

6 distinct bands in the Fe–S stretching region between 280 and 420 cm⁻¹ (Figure 1), with relative intensities quite similar to those for *Aa Fd5* (6) (and Figure 1) and Pdx (21). The strongest features in the natural abundance S resonance Raman of the former two proteins are at 288 cm⁻¹, assigned as the B_{3u}^t asymmetric Fe–S^t stretching mode, and at 351 cm⁻¹, assigned as the B_{3u}^b asymmetric Fe–S^b stretching mode. Despite the terminal and bridging labels (21), for both features we observe $\sim 5\text{--}7\text{ cm}^{-1}$ shifts with ^{36}S substitution in *Rc FdVI*. Given that we are using ^{36}S instead of ^{34}S , these shifts agree nicely with the 3.3 cm^{-1} shifts seen for these modes after ^{34}S substitution in Pdx (21). A simple Fe–S harmonic oscillator would shift $\sim 3.5\%$ between ^{32}S and ^{36}S , or $\sim 10\text{--}12\text{ cm}^{-1}$ shift in this region. The $\sim 2\%$ shifts

observed for these features indicate that in *Rc FdVI*, as in Pdx, there is substantial mixing of bridging S motion with terminal S (and/or other atom) motion in these modes.

Four other predominantly Fe–S stretching peaks are clear in the Raman data. The highest frequency ^{36}S -sensitive mode is at 421 cm⁻¹ and corresponds to the 426 cm⁻¹ band in Pdx (all of our spectra refer to ^{57}Fe proteins). The latter has been assigned as a B_{2u}^b asymmetric Fe–S^b stretching mode in idealized D_{2h} symmetry for the $\text{Fe}_2\text{S}_2\text{S}_4^t$ core (21), with the symmetry labels defined by placing the *x*-axis along the Fe–Fe vector and the *z*-axis normal to the Fe_2S_2^b plane. (Some earlier papers (60) used different *x*-axes, resulting in the permutation of the symmetry labels.) We observe a substantial ($\sim 14\text{ cm}^{-1}$) shift with ^{36}S substitution into the

Table 1: Mode Assignments and Calculated and Observed Fe–S Stretching Frequencies and ^{36}S Isotope Shifts for Oxidized *Rc* FdVI Using the C_{2h} Fe₂S₂(SCC)₄ Model

mode label			Pdx, ^b Ado, ^c and spinach ^d Raman		⁵⁷ Fe <i>Rc</i> FdVI Raman ^e		⁵⁷ Fe <i>Rc</i> FdVI NRVS ^e		calculated values		
D _{2h}	C _{2h}	C _{2v}	ν (cm ⁻¹)	$\Delta\nu$ ^{34}S (cm ⁻¹)	ν (cm ⁻¹)	$\Delta\nu$ ^{36}S (cm ⁻¹)	ν (cm ⁻¹)	$\Delta\nu$ ^{36}S (cm ⁻¹)	ν (cm ⁻¹)	$\Delta\nu$ ^{36}S (cm ⁻¹)	e_{Fe}^2
B _{2u} ^b	B _u ^b	B ₁	426 421 428	6.1 6.3 4.5	421	14	421	16	419.1	14.5	0.373
A _g ^b	A _g ^b	A ₁	400 393 397	5.0 5.6 4	395	11	393	11	392.5	11.8	0.345
B _{3u} ^b	B _u ^b	A ₁	350 349 369	3.3 3.2 3	351	6	352 (sh)		351.2	2.8	0.427
B _{1u} ^t	A _u ^t	B ₂	344 341 355	0.8 0.8 1.5	340 ^a		341	~0	335.0	0	0.386
B _{2g} ^t	B _g ^t	B ₂	344 341 340	0.8 0.8 2.5	340 ^a		341	~0	335.0	0	0.386
A _g ^t	A _g ^t	A ₁	338 329 340	2.7 1.5 2.5	329 ^a	5 ^a			316.7	3.6	0.041
B _{1g} ^b	A _g ^b	B ₁	320 317 330	3.3 3.2 3.0	320	8	321	8	314.4	8.6	0.450
B _{3u} ^t	B _u ^t	A ₁	291 291 285	3.3 3.3 4.5	288	5			286.9	7.4	0.057

^a Approximate value based on decomposition of broad feature at 335 cm⁻¹ (by analogy to Adx) and shifts in ^{36}S spectrum; sh = unresolved shoulder.
^b Ref 21. ^c Ref 22. ^d Ref 58. ^e This work.

bridging S position (Table 1), consistent with a relatively pure Fe–S^b stretching assignment. At slightly lower energy, we see the symmetric A_g^b Fe–S^b stretching mode at 395 cm⁻¹. For this mode, the ~11 cm⁻¹ shift with ^{36}S substitution is also consistent with a large component of bridging S motion. Two other clear maxima in the natural abundance S spectrum are at 320 cm⁻¹ and at ~335 cm⁻¹. The 320 cm⁻¹ band appears to shift to 312 cm⁻¹ with ^{36}S substitution, consistent with a B_{1g}^b symmetric Fe–S^b stretching assignment. However, the apparent 10–11 cm⁻¹ shift of the 335 cm⁻¹ peak to 324 cm⁻¹ seems large given the A_g^t and B_{1u}^t/B_{2g}^t Fe–S^t previous stretching assignments for this region.

On closer inspection, the band at ~335 cm⁻¹ is seen to be significantly broader than the other spectral features. With the closely related Adx protein, by using 406.9 nm excitation, Han and co-workers resolved two peaks at 329 and 341 cm⁻¹ in this region (22). In another similar protein, Pdx, a peak at 344 cm⁻¹ with 406.9 nm excitation was replaced by a 338 cm⁻¹ peak with 457.9 nm incident radiation (21). Thus, a plausible interpretation of our *Rc* FdVI Raman spectrum is that there are (at least) 2 unresolved modes in the ~335 cm⁻¹ region. By analogy with Adx and Pdx, we assume that one of these peaks has a 3–5 cm⁻¹ ^{36}S isotope shift to 324 cm⁻¹, while the other feature is assumed to have a small or negligible shift (Table 1).

Below the ice band at 230 cm⁻¹, a number of weak features corresponding to bending and torsional modes can be seen. In particular, a band at ~190 cm⁻¹ is apparent, both for *Rc* FdVI and especially for *Aa* Fd5. In model compound studies, Han and co-workers assigned similar bands at 197–210 cm⁻¹ as A_g^{Fe–Fe} stretching modes (24). At lower energies, we observed a feature at 131 cm⁻¹, which lacks a significant ^{36}S isotope shift and matches a band reported two decades ago by Meyer, Moulis, and Lutz (58). Finally, there appears to be a real band at 77 cm⁻¹ in the natural abundance S *Rc* FdVI Raman spectrum, but we were not able to observe this feature in the less concentrated ^{36}S -enriched *Rc* FdVI sample.

Resonance Raman spectra for reduced *Rc* FDVI are shown in Figure 2. These data strongly resemble previously published spectra for reduced Pdx (21). In contrast with the oxidized FdVI spectrum, only 4 clear ^{36}S -sensitive bands are observed, at 402, 381, 310, and 276 cm⁻¹ in the sample with natural abundance S. The band at 310 cm⁻¹ is broad and appears to split in the ^{36}S -substituted FdVI spectrum. As with other [2Fe-2S] Fds, the strong B_{3u}^t mode, now of A₁ symmetry, exhibits a modest ^{36}S -shift to lower energy, from 276 to 267 cm⁻¹. From the variation between 488 and 515 nm excitation, the next higher feature can tentatively be

decomposed into 2 bands at 308 and 315 cm⁻¹. This proposed splitting is confirmed as two resolved peaks at 301 and 309 cm⁻¹ in the ^{36}S Raman spectrum with 515 nm excitation. Two additional strong bands are seen at 381 and 402 cm⁻¹, and their shifts are summarized in Table 2.

NRVS. The ⁵⁷Fe PVDOS for oxidized and reduced *Rc* FdVI and *Aa* Fd5 are also presented in Figures 1 and 2, and the individual peak positions are listed in Tables 1 and 2. In contrast with previous rubredoxin NRVS data (61), where individual modes were not well-resolved, there are a number of sharp features in the oxidized *Rc* FdVI spectra. These include peaks at 421 cm⁻¹ and 393 cm⁻¹ that presumably correspond, respectively, to B_{2u}^b asymmetric Fe–S^b stretch and A_g^b Fe–S^b stretch modes. These bands exhibit large (16 or 11 cm⁻¹, respectively) ^{36}S isotope shifts (Figure 1) that are the same, within experimental error, as those seen in the Raman data. The fluctuations in the region above 420 cm⁻¹, where we do not expect significant NRVS, are a useful gauge of the experimental noise.

The strongest PVDOS features occur in a broad band between ~300 and 360 cm⁻¹. There are 2 peaks at 321 and 341 cm⁻¹, but the overall width suggests a number of unresolved bands. In the ^{36}S sample spectrum, peaks at ~310 and 290 cm⁻¹ emerge from under this envelope, presumably because some near degenerate modes shift more than others. In contrast with the resonance Raman, where the strongest feature is often the B_{3u}^t band at ~290 cm⁻¹, there is very little NRVS intensity in this region. This is consistent with the B_{3u}^t assignment because in this mode, attributed to an asymmetric combination of the two FeS₄ breathing modes (62), there is very little Fe motion.

Significant PVDOS amplitude also occurs between ~15 and 240 cm⁻¹ with a distinct local maximum at ~190 cm⁻¹ and an overall peak at ~78 cm⁻¹ (Figure 1). The 190 cm⁻¹ band, also seen in the *Rc* FdVI Raman, and similar bands at 197–210 cm⁻¹ in model compounds have been assigned as A_g^{Fe–Fe} stretching modes (24). The PVDOS features below 60 cm⁻¹ in both ^{36}S *Rc* FdVI spectra are most likely artifacts of background subtraction since the resolution was lower (~12 cm⁻¹) during the measurements for these samples.

In the spectra for the reduced protein, the high frequency band at 421 cm⁻¹ shifts down to 400 cm⁻¹, and the 393 cm⁻¹ feature moves to 382 cm⁻¹. Both of the reduced peaks show further ~15 cm⁻¹ shifts upon ^{36}S substitution. A group of broad features initially between ~300 and 360 cm⁻¹ moves to between ~270 and 340 cm⁻¹. An especially interesting peak is seen at ~276 cm⁻¹ in both the natural abundance and ^{36}S PVDOS. Johnson and co-workers

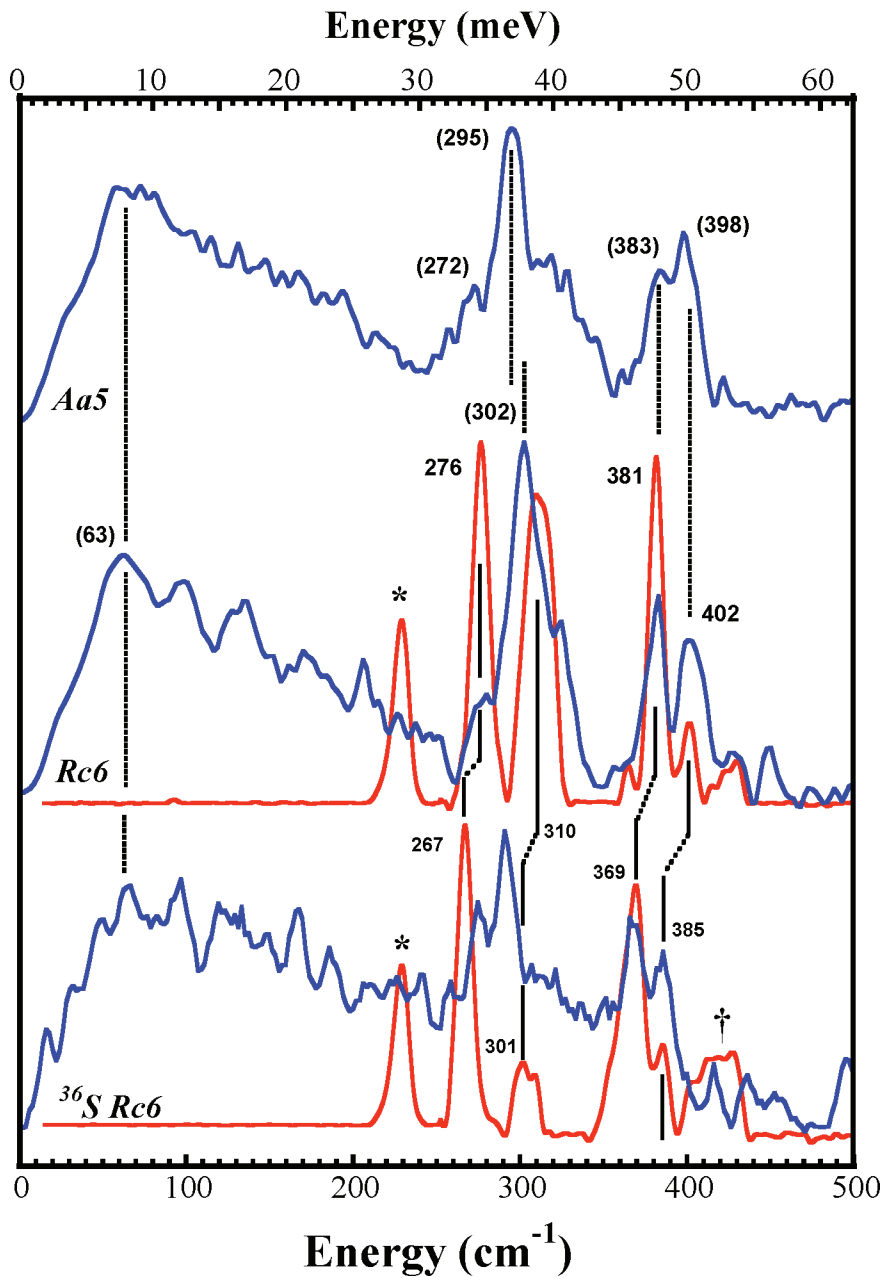


FIGURE 2: Top to bottom: resonance Raman spectra, using excitation at 515 nm (red line), compared with ⁵⁷Fe PVDOS (blue line) for reduced, ⁵⁷Fe-enriched (a) *Aa* Fd5, (b) *Rc* FdVI, and (c) ³⁶Sb-substituted *Rc* FdVI. * Marks ice band, and † marks possible dithionite decomposition product in Raman spectra. Dashed vertical lines highlight common PVDOS features between spectra; solid vertical lines mark Raman peak positions. Numbers in parentheses refer to PVDOS peaks; the remaining values are Raman peak positions.

Table 2: Mode Assignments and Calculated and Observed Fe–S Stretching Frequencies, ³⁶S Isotope Shifts for Reduced *Rc* FdVI Using the C_{2h} Fe₂S₂(SCC)₄ Model

mode label			Pdx, Ado Raman ^a		⁵⁷ Fe <i>Rc</i> FdVI Raman		⁵⁷ Fe <i>Rc</i> FdVI NRVS		calculated values		
D _{2h}	C _{2h}	C _{2v}	ν (cm ⁻¹)	$\Delta\nu$ ³⁴ S (cm ⁻¹)	ν (cm ⁻¹)	$\Delta\nu$ ³⁶ S (cm ⁻¹)	ν (cm ⁻¹)	$\Delta\nu$ ³⁶ S (cm ⁻¹)	ν (cm ⁻¹)	$\Delta\nu$ ³⁶ S (cm ⁻¹)	e_{Fe}^2
B _{2u} ^b	B _u ^b	B ₁	406 398	4.5 4.5	402	17	400	15	399.5	13.6	0.383
A _g ^b	A _g ^b	A ₁	381 377	4.2 4.5	381	13	382	15	380.9	14.7	0.278
B _{3u} ^b	B _u ^b	A ₁	307 307	3.0	315 (u)	6	314 (s)	7	304.4	2.5	0.257
B _{1u} ^t	A _u ^t	B ₂	319	0.6			324		326.2	0	0.373
B _{2g} ^t	B _g ^t	B ₂				302		303.1	0	0.354	
A _g ^t	A _g ^t	A ₁	307 307	3.0	308 (u)	7	306 (ss)	7	291.2	2.4	0.335
B _{1g} ^b	A _g ^b	B ₁	273 276	3.4 2.5			290 (ss)	7	282.1	7.2	0.433
B _{3u} ^t	B _u ^t	A ₁	273 276	3.4 2.5	276	9	276	8	269.6	7.2	0.040

^a Ref (21). s, shoulder; ss, small shoulder; u, unresolved.

predicted that the FeII-(S¹) stretch would occur in the region, but it lacked resonance Raman intensity (21).

Normal Mode Analysis. The resonance Raman spectra of [2Fe-2S] ferredoxins (21–23) and [Fe₂S₂(SR)₄]ⁿ⁻ model com-

Table 3: Comparison of Force Constants Used in Simulations of Oxidized and Reduced *Rc* FdVI vs Values Employed by Han et al. (22, 24)^a

<i>K</i>(Fe–S^b) (ox)	1.389 ^b 1.46 ^c 1.36 ^f 1.40 – Han a 1.131 ^b 1.18 ^c 1.07 ^f 1.20–Han a	<i>H</i>(Fe–S^b–Fe)	0.425 ^{b,c} 0.3 ^{d,e} 0.3 ^{f,g} 0.45–Han 0.3 ^{b,c} 0.15 ^{d,e} 0.41 ^{f,g} 0.40–Han	<i>K</i>(Fe · · Fe)	0.011 ^b 0.2 ^c 0.19–Han 0 ^{d,e} 0.149 ^b 0.124 ^c 0.09–Han 0.168 ^d 0.1 ^e
<i>K</i>(Fe^{II}–S^b)(red)	1.08 ^d 1.17 ^e 1.05 ^g 0.98–Han b	<i>H</i>(S^b–Fe–S^t)	0.1 ^{b,c} 0.1 ^{d,e} 0.24 ^{f,g} 0.38–Han	<i>f</i>(FeS^b–FeS^b)^h	0.001 ^b 0.069 ^c 0.07–Han 0.066 ^d 0.039 ^e
<i>K</i>(Fe^{II}–S^t)(red)	0.9 ^{d,e} 0.81 ^g 0.83–Han b	<i>H</i>(S^t–Fe–S^t)	0.3 ^{b,c} 0.3 ^{d,e} 0.22 ^{f,g} 0.35–Han	<i>f</i>(FeS^b–FeS^t)	0.01 ^b 0.043 ^c 0.08–Han 0.066 ^d 0.04 ^e
<i>K</i>(Fe^{III}–S^b)(red)	1.46 ^{d,e} 1.36 ^g	<i>H</i>(Fe–S–C)	0.3 ^{b,c} 0.4 ^{d,e} 0.35 ^{f,g} 0.35–Han	<i>f</i>(FeS^t–FeS^t)	-0.031 ^b 0.0 ^c 0.12–Han 0.008 ^d 0.01 ^e
<i>K</i>(Fe^{III}–S^t)(red)	1.055 ^d 1 ^e 1.07 ^g	<i>H</i>(S–C–C)(ox/red)	0.82 ^{b,e} 0.82–Han	<i>F</i>(S^t · · S^t)	0.325 ^b 0.218 ^c 0.12 ^{d,e}
<i>K</i>(S–C)	3.05 ^{b,e} 2.50–Han	<i>H</i>(S–C–H) (ox/red)	0.62 ^{c,e}	<i>F</i>(S^b · · S^b)	0.041 ^b 0.05 ^c 0.04 ^{d,e}
<i>K</i>(C–C)	4.80 ^{b,e} 4.80–Han	<i>H</i>(H–C–H) (ox/red)	0.62 ^{c,e}	<i>F</i>(S^b · · S^b)	0.015 ^b 0.0 ^c 0.025 ^{d,e}

^a See text for discussion of errors. ^b This work, C_{2h} Fe₂S₂(SCC)₄ for oxidized *Rc* FdVI. ^c This work, C₁ Fe₂S₂(S-cysXYZZ')₄ for oxidized *Rc* FdVI. ^d This work, C_{2h} Fe₂S₂(SCC)₄ for reduced *Rc* FdVI. ^e This work, C₁ Fe₂S₂(S-cysXYZZ')₄ for reduced *Rc* FdVI. ^f This work, full protein model for oxidized *Rc* FdVI. ^g This work, full protein model for reduced *Rc* FdVI. ^h Common atom is S^b. ⁱ Common atom is Fe; units for force constants: *K* = stretching (mdyn/Å), *H* = bending (mdyn Å/rad²), *F* = nonbonded interaction (mdyn/Å), *f* = stretch–stretch and stretch–bend interaction (mdyn/rad); Han: ref (24); Han–a: oxidized adrenodoxin parameter from ref (22); Han – b: reduced adrenodoxin parameter from ref (22).

plexes (24) have been interpreted with empirical force fields, and our analysis again relies on much of this body of work. As with previous rubredoxin NRVS studies (61), we began with small, high symmetry models, and we then progressively both increased the model size and lowered the symmetry. The calculated frequencies and ³⁶S isotope shifts for the high frequency normal modes of these simple models are compared with the experimental data in Tables 1 and 2, while the resulting parameters are summarized in Table 3. Comparisons between experimental and calculated *D*_{Fe}($\bar{\nu}$) for oxidized *Rc* FdVI are shown in Figure 3.

Fe₂S₂S'₄ Models. The simplest model for the redox active site is a Fe₂S₂S'₄ model in D_{2h} symmetry. This is a reasonable approximation for the geometry of the central Fe₂S₆ cluster (Chart 2). We started with this model and adjusted the Urey–Bradley force field parameters to match the main peaks in the experimental *D*_{Fe}($\bar{\nu}$) spectrum. As discussed previously for [Fe₂Cl₆]²⁻ (63) and [Fe₂S₂Cl₄]²⁻ (60, 64), this D_{2h} model yields 8 modes that are primarily Fe–X stretch in character, and 7 of these are NRVS-active.

The Fe–S stretching modes occur between 280 and 420 cm⁻¹. As deduced from empirical force fields (24) or DFT analysis (65), the highest frequency modes primarily involve more Fe–S^b motion, while the lowest frequency modes are mostly Fe–S^t in nature. We note that the 288 cm⁻¹ (B_{3u}^l) mode, which is often the strongest Raman feature, is essentially invisible in the NRVS data, indicating the lack of Fe kinetic energy in this mode. The lack of Fe motion in the B_{3u}^l mode was previously confirmed by the absence of

isotope shifts in model compounds substituted with ⁵⁴Fe (24). The eigenvector for this mode has been described as “concerted out-of-phase breathing motion of the linked FeS₄ tetrahedra” (22). Although differential H-bonding can lead to large resonance Raman intensity for this mode, most of the motion in this mode involves the sulfur atoms, and it is consequently weak in the NRVS. A similar absence of NRVS intensity (vs strong resonance Raman intensity) was observed for the FeS₄ breathing modes in oxidized and reduced rubredoxin (61).

Fe₂S₂(SCC)₄ Models. The orientation of the cysteine carbons, which is reflected in the Fe–S–C_β–C_α dihedral angle, has frequently been cited as a major determinant of the Fe–S stretching frequencies (66). Since the importance of coupling with cysteine side chain motion is well-documented, we proceeded with Fe₂S₂(SCC)₄ models in C_{2h} symmetry. The masses of the C_β and C_α carbons were increased to model the presence of 2 or 3 hydrogens, respectively. We again adjusted the Urey–Bradley force field parameters to maximize correspondence with the experimental *D*_{Fe}($\bar{\nu}$) spectrum for both natural abundance S and ³⁶S-bridge-substituted oxidized *Rc* FdVI, while at the same time reproducing as well as possible the observed Raman frequencies. As shown in Table 1, the calculated normal-mode frequencies for these Fe₂S₂(SCC)₄ models agree well with both the NRVS and Raman data, especially for the 393 and 421 cm⁻¹ (B_{2u}^b and A_g^b) modes that are predominantly Fe–S^b character. Below ~200 cm⁻¹ are modes that are primarily S–Fe–S bend and Fe–S–Fe bend in nature, along with torsional modes and vibrations involving

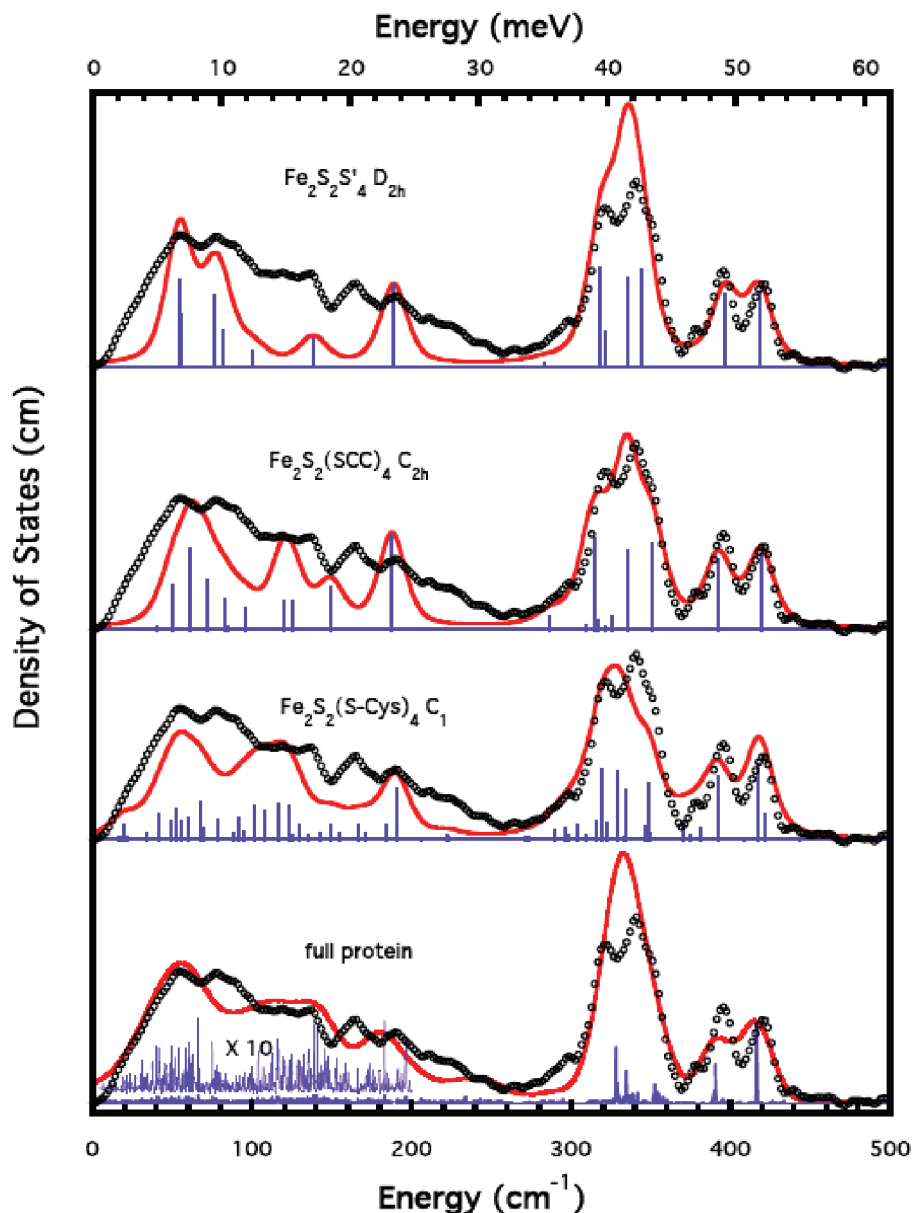


FIGURE 3: Simulations for oxidized *Rc* FdVI. Sticks represent intensities of individual normal modes. Top to bottom: ^{57}Fe PVDOS (○○○) and simulation (red line) for (a) $\text{Fe}_2\text{S}_2\text{S}'_4$ model in D_{2h} symmetry; (b) C_{2h} $\text{Fe}_2\text{S}_2(\text{SCC})_4$ model; (c) chromophore-in-protein model using crystal structure coordinates; (d) full protein analysis. In (a–c), PVDOS has been broadened with a 10 cm^{-1} Voigt profile (50% Gaussian, 50% Lorentzian, 10 cm^{-1} fwhm) to account for experimental and natural linewidths. In (d), an 8 cm^{-1} Gaussian broadening was used.

large-scale protein motion. In the $[\text{Fe}_2\text{S}_2\text{Cl}_4]^{2-}$ NRVS, several of these modes are clearly resolved, at 101, 145, and 177 cm^{-1} (64). However, in the *Aa* Fd5 and *Rc* FdVI PVDOS, there is instead a broad pyramid of intensity between 20 and 220 cm^{-1} . The C_{2h} symmetry small model simulation captures some of the local intensity maxima, but as expected, the calculation predicts narrower features than are actually observed.

A referee has inquired as to the significance of the parameters reported in Table 3. Since the stretching force constants are most important for the high frequency portion of the spectrum, we investigated how large a change in one parameter (with all other parameters fixed) was required to double the residual defined in eq 4, restricted to the region above 250 cm^{-1} . The stretching force constants for Fe and bridging sulfides, $K_{\text{Fe-S(b)}}$, and for Fe and terminal thiolate, $K_{\text{Fe-S(t)}}$, were the most constrained, to better than 0.5%, with the residuals doubling over intervals of $\pm 0.007 \text{ mdyne } \text{\AA}^{-1}$ and $\pm 0.008 \text{ mdyne } \text{\AA}^{-1}$, respectively. The error estimates for the bending force constants

used the entire NRVS data range because these parameters affect the lower frequency region. With these procedures, the bending force constants could be changed by $\pm 10\%$ before doubling the residual. All of these error estimates become several-fold larger if correlated parameters are allowed to float. We therefore note the point made some time ago by Spiro and co-workers: “Although agreement with observation cannot be taken as proof that the force field is correct, the accurate calculation of isotope shifts does imply that the calculated eigenvectors are good approximations to the normal modes (67).” In the current set of experiments, the ^{36}S shifts help define the amount of bridging S motion in a given normal mode, while the NRVS intensity constrains the amount of ^{57}Fe motion in the same.

Chromophore in Protein Models. In order to better capture the coupling between [2Fe-2S] cluster modes and the protein side chain motion, we further expanded our model to include all of the ligand cysteine atoms, as well as the carbonyl C and O of the residue adjacent to the cysteine N, and the amide

N of the residue bound to the cysteine carbonyl. The symmetry was relaxed to C₁, and all atoms were placed at the crystal structure coordinates. Initial values for the force constants associated with these peripheral atoms were obtained from the CHARMM molecular modeling software (68). This approach was employed by Qiu and co-workers in their chromophore in protein calculations (69), who included all of the protein atoms in their model for plastocyanin, but assigned masses of 999 to polypeptide atoms more than 6 atoms away (via the ligating side chain) from the central Cu. The force constants for the core atoms were again optimized, with respect to both oxidized and reduced PVDOS (Table 3). The resultant $K_{\text{Fe-S(t)}}$ for the oxidized protein was 1.18 mdyne Å⁻¹, comparable to the 1.20 mdyne Å⁻¹ used by Han and co-workers, or for rubredoxin work, the 1.27 mdyne Å⁻¹ used by Czernuszewicz et al. (27) and the 1.36 mdyne Å⁻¹ value used by Saito and co-workers (70). For $K_{\text{Fe-S(b)}}$, our value 1.46 mdyne Å⁻¹ is slightly larger than the 1.40 mdyne Å⁻¹ used by Han and co-workers, and this may be due to the higher B_{2u}^b mode frequency observed for oxidized *Rc FdVI*. The bending force constants, $H_{\text{S(b)FeS(b)}}$ and $H_{\text{S(t)FeS(t)}}$ were 0.3 mdyne-Å, compared to the 0.35 or 0.43 mdyne-Å values, respectively, used by Czernuszewicz (27) or Saito (70). Both of these groups were much less concerned with the bending mode region of the spectrum. As seen in Figure 3, the widths and intensities of the spectral features in the Fe–S stretching region above 300 cm⁻¹ are reasonably well captured by this model. However, the simulation below 260 cm⁻¹ remains too structured and is missing intensity. This suggests that, as argued previously (22), the Fe–S stretching modes are indeed localized to the cluster and cysteine ligands, while the bending and torsional modes of the clusters are more coupled to the protein and delocalized, and a larger model is needed to simulate this region.

Full Protein Calculations. Low frequency modes (<100 cm⁻¹) have not been observed before in [2Fe-2S] ferredoxins. In blue Cu proteins (71, 72) and heme proteins (73–75), modes between 20 and 80 cm⁻¹ have been referred to as phonon-like (76) or as delocalized mode(s) involving the protein skeleton motion (77). In Fe₂X₆ clusters, a number of low frequency cluster modes, such as MX₂ wag, twist, rock, and ring puckering, have also been predicted for the region below 100 cm⁻¹ (63), but for technical reasons, they have never been observed in bioinorganic Fe–S clusters. In Fe–S proteins, these low frequency cluster modes could be expected to couple to the many protein modes of comparable frequency. At the lowest end of the spectrum, collective motion of large segments of polypeptide might carry the cluster as a whole body, similar to the acoustic modes seen for lower molecular weight complexes.

To better model and characterize the low frequency region of the spectrum, the normal modes were calculated for a model with all of the protein atoms, along with 56 water molecules, as shown in Figure 5. These calculations used CHARMM22 parameters for the protein and initially used the Fe–S parameters from the D_{2h} Fe₂S₂(SCC)₄ model for the cluster. The Fe–S force constants were then adjusted manually to optimize the agreement between calculated and observed PVDOS. Of course, before the CHARMM normal mode calculation, the protein coordinates from the X-ray crystal structure were refined to minimize the energy in the

CHARMM22 force field, and thus, the small model Vibratz calculations and the total protein CHARMM calculations actually use slightly different structures for the [2Fe–2S] cluster site. This is one fundamental reason why the force constants are not perfectly transferable between the two calculations. Furthermore, the best Fe–S parameters for Vibratz and CHARMM are necessarily different because the force fields are quite different. The CHARMM22 force field has Coulombic and van der Waals terms (some of which indirectly incorporate hydrogen bonding) that are absent from the Vibratz Urey–Bradley force field.

The results demonstrate that the protein influence on the NRVS can be modeled without adjusting any polypeptide parameters. Since we have left the polypeptide part of the CHARMM22 force field unchanged, our final PVDOS prediction for this region is a natural consequence of the coupling of [2Fe-2S] cluster modes with low frequency protein modes.

We have used the eigenvectors from the full protein CHARMM calculation to illustrate the differences between different regions of the PVDOS spectrum (Figure 5). We chose a few specific modes for a variety of reasons. The 13 and 14 cm⁻¹ modes were chosen because they are highly collective protein modes that also contain a large amount of coherent [2Fe-2S] cluster motion. The 288 cm⁻¹ mode was chosen because it is the strongest band in the resonance Raman spectrum. Finally, the 416 cm⁻¹ mode was chosen because it is the highest frequency mode with significant NRVS intensity. Animations of these motions are available as Supporting Information.

The lowest frequency eigenvectors, exemplified by the modes at ~13–14 cm⁻¹, involve delocalized protein skeleton motion and in-phase motion of the entire Fe₂S₂T₄ unit as a nearly rigid body (Figure 5). For the 13 cm⁻¹ mode, concerted motion of the Fe–S cluster along with the nearby polypeptide is coupled to motion of the C-terminus and nearby residues such that the two parts of the proteins move in opposite directions in a large-scale stretching motion (Figure 5a). For the 14 cm⁻¹ mode, concerted motion of the [2Fe-2S] cluster along with nearby residues is countered by motion of polypeptide near the N terminus (Figure 5b). Higher frequency modes, such as those at 288 and 416 cm⁻¹, exhibit much more localized motion of the [2Fe-2S] cluster. Of special interest is the mode at 288 cm⁻¹ (Figure 5c), previously assigned as an out-of-phase breathing motion of the two connected FeS₄ tetrahedra (24). This mode has virtually no Fe motion so that it is nearly invisible by NRVS, despite being the strongest feature in the resonance Raman spectra. In contrast, the mode at 416 cm⁻¹ (Figure 5d) is relatively weak in the Raman but has significant NRVS intensity due to Fe movement in the Fe–S^b stretching motion.

Reduced *Rc FdVI*. The analysis for reduced *Rc FdVI* followed lines similar to those used for the oxidized sample. For the Fe₂S₂(SCC)₄ models, the atomic coordinates used C_{2h} symmetry, but to allow for inequivalent Fe(II) and Fe(III) sites, we used C₁ symmetry for the normal mode calculations. The resulting comparisons between experimental and calculated $D_{Fe}(\bar{\nu})$ for reduced *Rc FdVI* are shown in Figure 4. For the Fe(III) site, the optimized Fe–S^t stretch force constant was found to be ~1 mdyne Å⁻¹, slightly lower than the 1.18 mdyne Å⁻¹ value used in the oxidized cluster simulation. The Fe(III)–S^b stretch force constant derived for

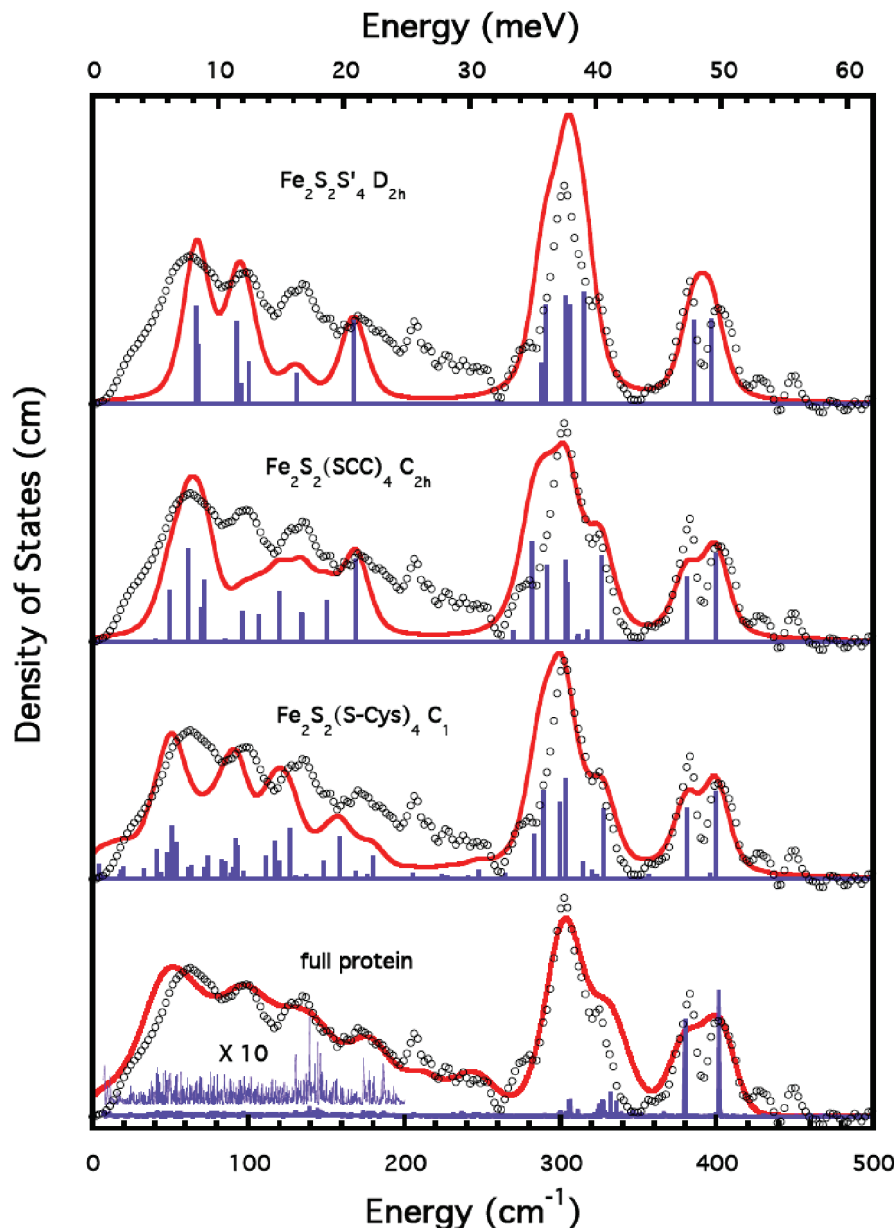


FIGURE 4: Simulations for reduced *Rc* FdVI. Top to bottom: ^{57}Fe PVDOS (•••) and simulation (red line) for (a) $\text{Fe}_2\text{S}_2\text{S}'_4$ model in D_{2h} symmetry; (b) C_{2h} $\text{Fe}_2\text{S}_2(\text{SCC})_4$ model; (c) chromophore-in-protein model using crystal structure coordinates; (d) full protein normal-mode analysis. In (a–c), calculated PVDOS has been broadened with a 10 cm^{-1} Voigt profile (50% Gaussian, 50% Lorentzian, and 10 cm^{-1} fwhm) to account for experimental and natural linewidths. In (d), an 8 cm^{-1} Gaussian broadening was used.

the partially reduced cluster was unchanged (both at $1.46 \text{ mdyne } \text{\AA}^{-1}$). For the Fe(II) site, significantly smaller Fe–S^t and Fe–S^b stretch force constants were found: $0.9 \text{ mdyne } \text{\AA}^{-1}$ and $1.17 \text{ mdyne } \text{\AA}^{-1}$, respectively. A 31% diminution, from 1.24 down to $0.92 \text{ mdyne}/\text{\AA}$, was previously observed between oxidized and reduced rubredoxin (61). Our results are also in accord with the 30% reduction of $K_{\text{Fe-S}}$ inferred for the Fe(II) site in 2-Fe ferredoxins from the resonance Raman of the reduced forms (22). In contrast, we found that the bend force constants $H_{\text{S-Fe-S}}$ are about the same for both oxidized and reduced *Rc* FdVI.

Localization of Normal Modes. As illustrated in Figures 3 and 4, progressively larger models for the environment of Fe in oxidized or reduced *Rc* FdVI produce better simulations of the ^{57}Fe PVDOS, especially in the low frequency regions. The normal mode calculations for even the simplest model, the D_{2h} $\text{Fe}_2\text{S}_2\text{S}'_4$ construct, adequately capture both the intensity and the frequency of the two highest energy features. These modes,

assigned as B_{2u} and A_g in D_{2h} symmetry, are found to be highly localized on the cluster, even when the model is expanded to the full protein structure (Figure 5).

Only the full protein calculations accurately capture the breadth of the spectra below 260 cm^{-1} . Since the NRVS intensity is proportional to the fraction of kinetic energy from ^{57}Fe in a given normal mode, this reflects the fact that Fe motion is divided between a large number of modes that involve progressively larger numbers of atoms. The degree of localization of Fe–S modes in rubredoxins and ferredoxins has been the subject of discussion for some time (22, 26, 27, 70, 78). To better illustrate this issue on a quantitative basis, we evaluated the degree of collectivity κ for the normal modes of *Rc* FdVI, and the results are presented in Figure 6.

The overall collectivity trend that we see for *Rc* FdVI (Figure 6) is quite similar to that observed in the original calculations for the small (46 amino acid) protein crambin (56). The collectivity values occur in a broad band, rising

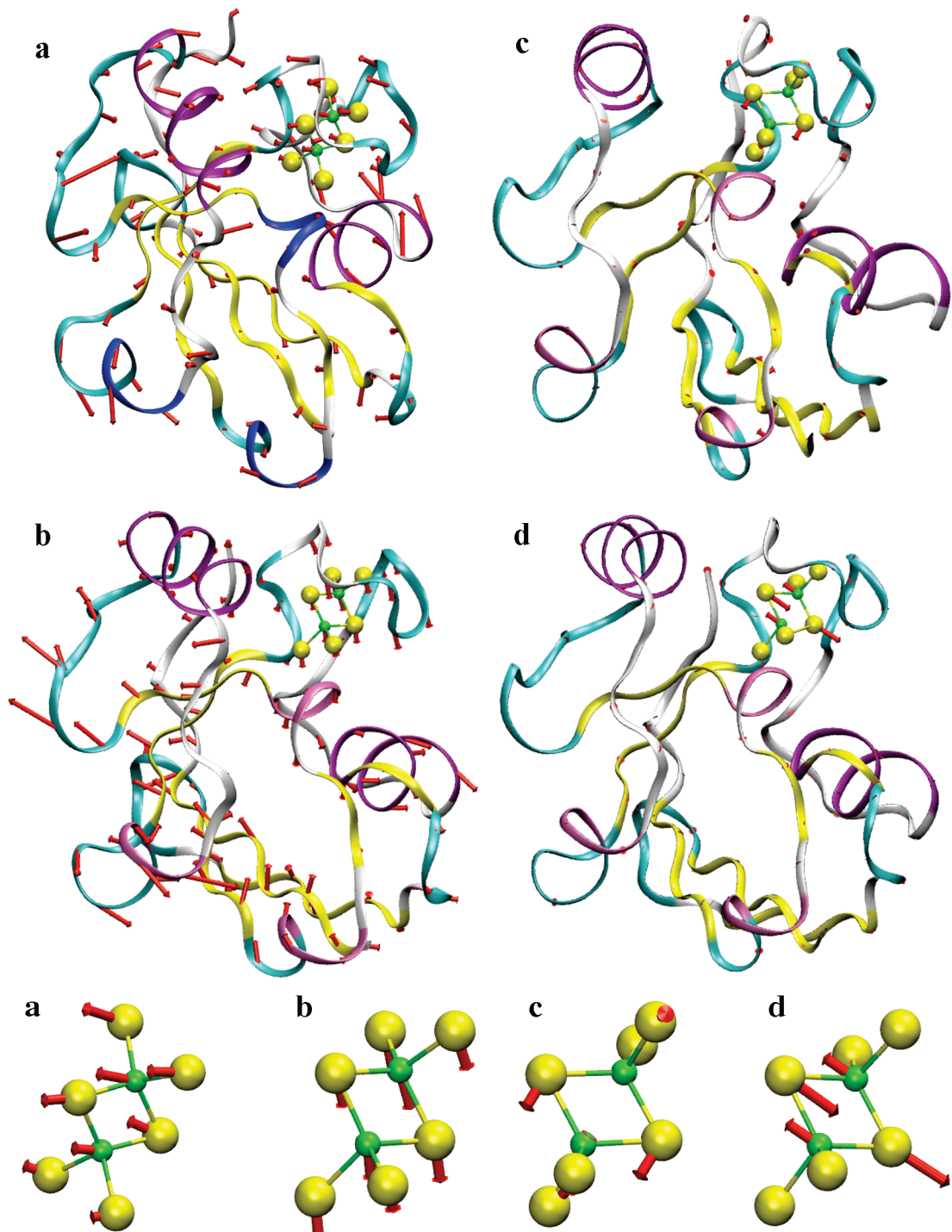


FIGURE 5: Illustration of molecular motion in normal modes derived from full protein analysis. Arrows represent relative magnitude and directions of C α or cluster atom motion in oxidized Rc FdVI. Modes illustrated are (a) 13 cm $^{-1}$, (b) 14 cm $^{-1}$, (c) 288 cm $^{-1}$, and (d) 416 cm $^{-1}$. Figures were made with VMD (10).

from a range of $\sim 0.2\text{--}0.4$ (with some outliers) at 200 cm $^{-1}$ to $\sim 0.4\text{--}0.6$ for the lowest frequencies. As noted by Tama and Sanejouand, κ is analogous to the W term in Boltzmann's $S = k \log W$, and it is a measure of the degree of participation of all the atoms in a particular conformational change or normal mode. Thus, if all of the atoms have equal amounts of motion, $\kappa = 1$, and in the limit that only a single atom moves, $\kappa = 1/N$, where in our case N is the number of non-hydrogen protein atoms (797) plus 4 (for the atoms in the cluster). If the number of atoms involved in the normal mode is taken as κN , then these calculations show that the lowest frequency

modes around 10–20 cm $^{-1}$ are extensively delocalized over almost half or more of the polypeptide atoms.

At the other extreme, we found that the highest frequency cluster mode, calculated at a frequency of 416 cm $^{-1}$ and illustrated in Figure 5, is quite localized. This mode, assigned as the B_{2u} Fe–S stretch in the D_{2h} symmetry model, had a value of $\kappa = 0.0092$, suggesting the involvement of ~ 7.5 atoms. This corresponds nicely to the view of this mode as localized on the Fe₂S₂S'₄ core, and is in agreement with the strong NRVS and the large ³⁶S isotope shift. The calculations suggest, however, that mode delocalization increases quite rapidly for lower frequencies. For a pair of modes at 390

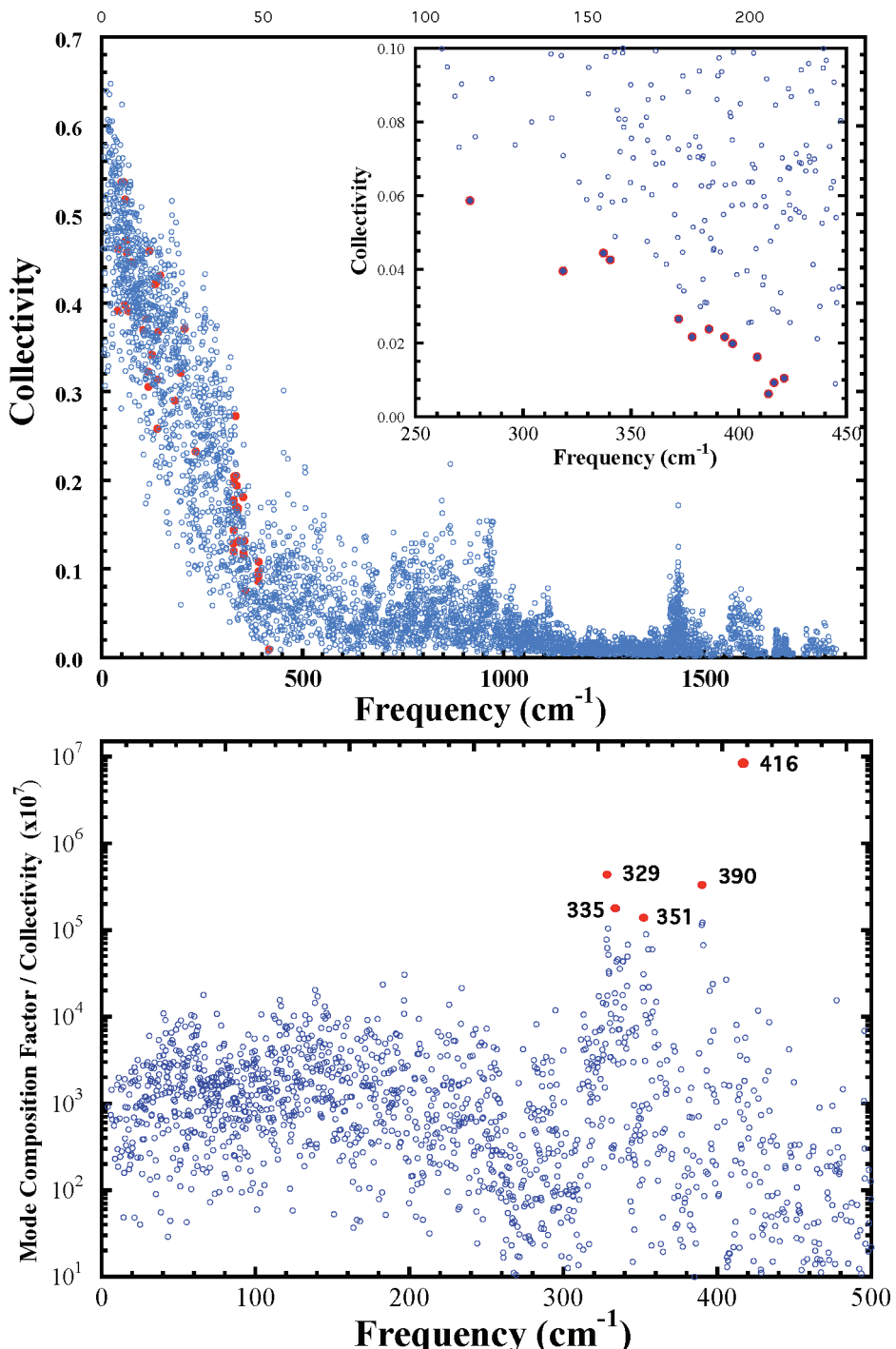


FIGURE 6: Top: degree of collectivity (κ) for normal modes of oxidized *Rc* FdVI. Modes with largest mode composition factors are highlighted (red circles). In the inset, the highlighted modes (filled circles) are simply those with the lowest κ . Bottom: the mode composition factor divided by κ , to emphasize cluster-centered normal modes.

cm^{-1} , corresponding to the A_g motion in D_{2h} symmetry. $\kappa = 0.086$ or 0.092 , corresponding to $70-74$ atoms, while a strong NRVS mode at 352 cm^{-1} , corresponding approximately to B_{3u}^b motion, has $\kappa = 0.11$. These values imply the involvement of all 4 cysteine residues as well as some neighboring atoms. Extensive delocalization of modes involving cysteine thiolates was inferred from the observation of ^{15}N isotope shifts in the resonance Raman spectra of *Anabaena* ferredoxin (32). The CHARMM calculations suggest that even some nominally Fe–S^b modes can be quite delocalized. Finally, the bend modes in the $100-200 \text{ cm}^{-1}$ range have $\kappa > 0.25$, showing that these motions are

extensively coupled with the motion of more than two dozen amino acids. We are currently exploring the relationship between the more collective normal modes and the conformational changes between oxidized and reduced 2Fe-2S ferredoxins.

SUMMARY

The combined application of ^{57}Fe NRVS and resonance Raman spectroscopy, along with ^{36}S labeling and full protein normal-mode analysis, has provided a broader view of 2Fe-2S cluster dynamics in ferredoxin electron transfer proteins.

For oxidized *Rc* FdVI and *Aa* Fd5, additional modes are seen that are difficult to observe by Raman, including strong features below 100 cm⁻¹. Furthermore, in the reduced protein, the Fe(II) site is equally accessible to the NRVS method, whereas the Raman is primarily sensitive to Fe(III) dynamics.

A special feature of NRVS is the potential for accurate intensity calculations; the amplitude of NRVS features reveals the fraction of kinetic energy due to Fe motion in a particular normal mode. Combined with its ability to observe low frequency modes, the NRVS data has allowed us to construct an empirical force field that also includes Fe-based bending and torsional motions. The coupling of cluster modes with protein motion has been successfully modeled by adding our empirical Fe–S force constants to the CHARMM force field (without modification of the polypeptide parameters). Future studies will explore the relationship between low frequency normal modes and redox-induced conformational changes in ferredoxins.

ACKNOWLEDGMENT

We thank Yves Jouanneau for supplying the plasmid (pJA66) for expression of *Rc* FdVI.

SUPPORTING INFORMATION AVAILABLE

Raman data and torsion angle for some [2Fe–2S] ferredoxins are summarized in Table S1. Figure S1 shows experimental data for the average separation of B_{3u}^t mode and A_g^t, B_{2g}^t, and B_{3u}^b modes vs the average Fe-S-C-C dihedral angle. Figures S2 and S3 show simulations of ³⁶S data. Movies S1–S4 are animations of protein motions listed in Figure 5. This material is available free of charge via the Internet at <http://pubs.acs.org>.

REFERENCES

- Meyer, J. (2008) Iron-sulfur protein folds, iron-sulfur chemistry, and evolution. *J. Biol. Inorg. Chem.* 13, 157–170.
- Bertini, I., Luchinat, C., Provenzani, A., Rosato, A., and Vasos, P. R. (2002) Browsing gene banks for Fe₂S₂ ferredoxins and structural modeling of 88 plant-type sequences: an analysis of fold and function. *Proteins* 46, 110–127.
- Fukuyama, K. (2004) Structure and function of plant-type ferredoxins. *Photosynth. Res.* 81, 289–301.
- Hajirezaei, M.-R., Peisker, M., Tschiersch, H., Palatnik, J. F., Valle, E. M., Carrillo, N., and Sonnewald, U. (2002) Small changes in the activity of chloroplastic NADP⁺-dependent ferredoxin oxidoreductase lead to impaired plant growth and restrict photosynthetic activity of transgenic tobacco plants. *Plant J.* 29, 281–293.
- Lange, H., Kaut, A., Kispal, G., and Lill, R. (2000) A mitochondrial ferredoxin is essential for biogenesis of cellular iron-sulfur proteins. *Proc. Natl. Acad. Sci. U.S.A.* 97, 1050–1055.
- Mitou, G., Higgins, C., Wittung-Stafshede, P., Conover, R. C., Smith, A. D., Johnson, M. K., Gaillard, J., Stubna, A., Münck, E., and Meyer, J. (2003) An Isc-type extremely thermostable [2Fe–2S] ferredoxin from *Aquifex aeolicus*. Biochemical, spectroscopic, and unfolding studies. *Biochemistry* 42, 1354–1364.
- Armengaud, J., Meyer, C., and Jouanneau, Y. (1997) A [2Fe–2S] Ferredoxin (FdVI) Is Essential for growth of the photosynthetic bacterium *Rhodobacter capsulatus*. *J. Bacteriol.* 179, 3304–3309.
- Sainz, G., Jakoncic, J., Sieker, L. C., Stojanoff, V., Sanishvili, N., Asso, M., Bertrand, P., Armengaud, J., and Jouanneau, Y. (2006) Structure of a [2Fe–2S] Ferredoxin from *Rhodobacter capsulatus* likely involved in Fe-S cluster biogenesis and conformational changes upon reduction. *J. Biol. Inorg. Chem.* 11, 235–246.
- Kakuta, Y., Horio, T., Takahashi, Y., and Fukuyama, K. (2001) Crystal structure of *Escherichia coli* Fdx, an adrenodoxin-type ferredoxin involved in the assembly of iron-sulfur clusters. *Biochemistry* 40, 11007–11012.
- Humphrey, W., Dalke, A., and Schulten, K. (1996) VMD—visual molecular dynamics. *J. Mol. Graphics* 14, 33–38.
- DeLano, W. L. (2002) The PyMOL Molecular Graphics System, DeLano Scientific LLC, Palo Alto, CA.
- Morales, R., Charon, M. H., Hudry-Clergeon, G., Pétilot, Y., Norager, S., Medina, M., and Frey, M. (1999) Refined X-ray structures of the oxidized, [2Fe–2S] ferredoxin from the cyanobacterium at 1.17 Å reduced at 1.3 Å, and *Anabaena* PCC7119 show redox-linked conformational changes. *Biochemistry* 38, 15764–15773.
- Müller, A., Müller, J. J., Müller, Y. A., Uhlmann, H., Bernhardt, R., and Heinemann, U. (1998) New aspects of electron transfer revealed by the crystal structure of a truncated bovine adrenodoxin, Adx(4–108). *Structure* 6, 269–280.
- Beilke, D., Weiss, R., Lohr, F., Pristovsek, P., Hannemann, F., Bernhardt, R., and Ruterjans, H. (2002) A new electron transport mechanism in mitochondrial steroid hydroxylase systems based on structural changes upon the reduction of adrenodoxin. *Biochemistry* 41, 7969–7978.
- Seviroukova, I. F., Garcia, C., Li, H. Y., Bhaskar, B., and Poulos, T. L. *J. Mol. Biol.* (2003) Crystal structure of putidaredoxin, the [2Fe–2S] component of the P-450_{cam} monooxygenase system from *Pseudomonas putida*. *J. Mol. Biol.* 333, 377–392.
- Pizzutti, F., Sétif, P., and Marchi, M. (2004) Theoretical investigation of the “CO in”–“CO out” isomerization in a [2Fe–2S] ferredoxin: free energy profiles and redox states. *J. Am. Chem. Soc.* 125, 15224–15232.
- Shakya, S. K., Gu, W., and Helms, V. (2005) Molecular dynamics simulation of truncated bovine adrenodoxin. *Biopolymers* 78, 9–20.
- Hintz, M. J., Mock, D. M., Peterson, L. L., Tuttle, K., and Peterson, J. A. (1982) Equilibrium and kinetic studies of the interaction of cytochrome P-450_{cam} and putidaredoxin. *J. Biol. Chem.* 257, 14324–14332.
- Pochapsky, T. C., Kostic, M., Jain, N., and Pejchal, R. (2001) Redox-dependent conformational selection in a Cys₄Fe₂S₂ ferredoxin. *Biochemistry* 40, 5602–5614.
- Jain, N., and Pochapsky, T. C. (1999) A new assignment strategy for the hyperfine-shifted ¹³C and ¹⁵N resonances in Fe₂S₂ ferredoxins. *Biochem. Biophys. Res. Commun.* 258, 54–59.
- Fu, W., Drozdowski, P. M., Davies, M. D., Sligar, S. G., and Johnson, M. K. (1992) Resonance Raman and magnetic circular dichroism studies of reduced [2Fe–2S] proteins. *J. Biol. Chem.* 267, 15502–15510.
- Han, S., Czernuszewicz, R. S., Kimura, T., Adams, M. W. W., and Spiro, T. G. (1989) Fe₂S₂ protein resonance raman revisited: structural variations among adrenodoxin, red paramagnetic protein ferredoxin. *J. Am. Chem. Soc.* 111, 3505–3511.
- Meyer, J., Clay, M. D., Johnson, M. K., Stubna, A., Münck, E., Higgins, C., and Wittung-Stafshede, P. (2002) A hyperthermophilic plant-type [2Fe–2S] ferredoxin from *Aquifex aeolicus* is stabilized by a disulfide bond. *Biochemistry* 41, 3096–3108.
- Han, S., Czernuszewicz, R. S., and Spiro, T. G. (1989) Vibrational spectra and normal mode analysis for [2Fe–2S] protein analogues using ³⁴S, ⁵⁴Fe, and ²H substitution: coupling of Fe-S Stretch and S-C-C bending modes. *J. Am. Chem. Soc.* 111, 3496–3504.
- Yachandra, V. K., Hare, J., Moura, I., and Spiro, T. G. (1983) Resonance Raman spectra of rubredoxin, desulforedoxin, and the synthetic analogue Fe(S₂-o-xyl)₂[–]: conformational effects. *J. Am. Chem. Soc.* 105, 6455–6461.
- Czernuszewicz, R. S., LeGall, J., Moura, I., and Spiro, T. G. (1986) Resonance Raman spectra of rubredoxin: new assignments and vibrational coupling mechanism from Iron-54/Iron-56 isotope shifts and variable wavelength excitation. *Inorg. Chem.* 26, 696–700.
- Czernuszewicz, R. S., Kilpatrick, L. K., Koch, S. A., and Spiro, T. G. (1994) Resonance Raman spectroscopy of iron(III) tetrathiolate complexes: implications for the conformation and force field of rubredoxin. *J. Am. Chem. Soc.* 116, 1134–1141.
- Fukuyama, K., Ueki, N., Nakamura, H., Tsukihara, T., and Matsubara, H. (1995) Tertiary structure of [2Fe–2S] ferredoxin from *Spirulina platensis* refined at 2.5 Å resolution: structural comparisons of plant-type ferredoxins and an electrostatic potential analysis. *J. Biochem.* 117, 1017–1023.
- Seviroukova, I. F. J. (2005) Redox-dependent structural reorganization in putidaredoxin, a vertebrate-type [2Fe–2S] ferredoxin from *Pseudomonas putida*. *Mol. Biol.* 347, 607–621.
- Vidakovic, M. S., Fraczkiewicz, G., and Germanas, J. P. (1996) Expression and spectroscopic characterization of the hydrogeno-

- somal [2Fe-2S] ferredoxin from the protozoan *Trichomonas vaginalis*. *J. Biol. Chem.* 271, 14734–14749.
31. Crossnoe, C. R., Germanas, J. P., LeMagueres, P., Mustata, G., and Krause1, K. L. (2002) The crystal structure of *Trichomonas vaginalis* ferredoxin provides insight into metronidazole activation. *J. Mol. Biol.* 318, 503–518.
 32. Rottaert, F. A., Pikus, J. D., Fox, B. G., Markley, J. L., and Sanders-Lohr, J. (2003) N-isotope effects on the Raman spectra of Fe₂S₂ ferredoxin and Rieske ferredoxin: evidence for structural rigidity of metal sites. *J. Biol. Inorg. Chem.* 8, 318–326.
 33. Rypniewski, W. R., Oh, B. H., Markley, J. L., Rayment, I., and Holden, H. M. (1991) Crystallization and structure determination to 2.5 Å resolution of the [2Fe-2S] ferredoxin isolated from *Anabaena* 1710. *Biochemistry* 30, 4126–4131.
 34. Kounosu, A., Li, Z., Cosper, N. J., Shokes, J. E., Scott, R. A., Imai, T., Urushiyama, A., and Iwasaki, T. (2004) Engineering a three-cysteine, one-histidine ligand environment into a new hyperthermophilic Archaeal Rieske-type [2Fe-2S] ferredoxin from *Sulfolobus solfataricus*. *J. Biol. Chem.* 279, 12519–12528.
 35. Williams, R. J. P. (1978) The conformational mobility of proteins and its functional significance. *Biochem. Soc. Trans.* 6, 1123–1126.
 36. Carlson, Curtis, E. H., Trewella, J., and Heidorn, D. B. (1988) Differences in the solution structures of oxidized and reduced cytochrome c measured by small-angle X-ray scattering. *Biochemistry* 27, 1121–1125.
 37. Morales, R., Charon, M. H., Kachalova, G., Serre, L., Medina, M., Gomez-Moreno, C., and Frey, M. (2000) A redox-dependent interaction between two electron-transfer partners involved in photosynthesis. *EMBO Rep.* 1, 271–276.
 38. Tezcan, F. A., Kaiser, J. T., Mustafi, D., Walton, M. Y., Howard, J. B., and Rees, D. C. (2005) Nitrogenase complexes: multiple docking sites for a nucleotide switch protein. *Science* 309, 1377–1380.
 39. Johnson, D. C., Dean, D. R., Smith, A. D., and Johnson, M. K. (2005) Structure, function, and formation of biological iron-sulfur clusters. *Annu. Rev. Biochem.* 74, 247–281.
 40. Dos Santos, P. C., Dean, D. R., Hu, Y., and Ribbe, M. W. (2004) Formation and insertion of the nitrogenase iron-molybdenum cofactor. *Chem. Rev.* 104, 1159–1173.
 41. Böck, A., King, P. W., Blokesch, M., and Posewitz, M. C. (2006) Maturation of hydrogenases. *Adv. Microb. Physiol.* 51, 1–225.
 42. Alp, E., Sturhahn, W., Toellner, T. S., Zhao, J., Hu, M., and Brown, D. E. (2002) Vibrational dynamics studies by nuclear resonant inelastic X-Ray scattering. *Hyperfine Interact.* 144/145, 3–20.
 43. Sturhahn, W. (2004) Nuclear resonant spectroscopy. *J. Phys.: Condens. Matter* 16, S497–S530.
 44. Leu, B. M., Zgierski, M. Z., Wyllie, G. R. A., Scheidt, W. R., Sturhahn, W., Alp, E. E., Durbin, S. M., and Sage, J. T. (2004) Quantitative vibrational dynamics of iron in nitrosoyl porphyrins. *J. Am. Chem. Soc.* 126, 4211–4227.
 45. Sturhahn, W., Toellner, T. S., Alp, E. E., Zhang, X., Ando, M., Yoda, Y., Kikuta, S., Seto, M., Kimball, C. W., and Dabrowski, B. (1995) Phonon density of states measured by inelastic nuclear resonant scattering. *Phys. Rev. Lett.* 74, 3832–3835.
 46. Sage, J. T., Paxson, C., Wyllie, G. R. A., Sturhahn, W., Durbin, S. M., Champion, P. M., Alp, E. E., and Scheidt, W. R. (2001) Nuclear resonance vibrational spectroscopy of a protein active-site mimic. *J. Phys.: Condens. Matter* 13, 7707–7722.
 47. Sturhahn, W. (2000) CONUSS and PHOENIX: evaluation of nuclear resonant scattering data. *Hyperfine Interact.* 125, 149–172.
 48. Chumakov, A. I., Rüffer, R., Leupold, O., and Sergueev, I. (2003) Insight to dynamics of molecules with nuclear inelastic scattering. *Struct. Chem.* 14, 109–119.
 49. Meyer, J. (1986) High-yield chemical assembly of [2Fe-2X] ($X = S, Se$) clusters into spinach apoferedoxin: product characterization by resonance Raman spectroscopy. *Biochim. Biophys. Acta* 871, 243–249.
 50. Toellner, T. (2000) Monochromatization of synchrotron radiation for nuclear resonant scattering experiments. *Hyperfine Interact.* 125, 3–28.
 51. Yoda, Y., Yabashi, M., Izumi, K., Zhang, X. W., Kishimoto, S., Kitao, S., Seto, M., Mitsui, T., Harami, T., Imai, Y., and Kikuta, S. (2001) Nuclear resonant scattering beamline at SPring-8. *Nucl. Instrum. Methods A* 467, 715–718.
 52. Shape Software, <http://www.shapesoftware.com/>.
 53. Dowty, E. (1987) Fully automated microcomputer calculation of vibrational spectra. *Phys. Chem. Minerals* 14, 67–79.
 54. Engeln-Mueller, G., and Uhlig, F. (1996) *Numerical Algorithms with C*, Springer-Verlag, New York.
 55. Brooks, B. R., Bruccoleri, R. E., Olafson, B. D., States, D. J., Swaminathan, S., and Karplus, M. (1983) CHARMM: A program for macromolecular energy, minimization, and dynamics calculations. *J. Comput. Chem.* 4, 187–217.
 56. Bruschweiler, R. (1995) Collective protein dynamics and nuclear spin relaxation. *J. Chem. Phys.* 102, 3396–3403.
 57. Tama, F., and Sanejouand, Y.-H. (2001) Conformational changes of proteins arising from normal mode calculations. *Protein Eng.* 14, 1–6.
 58. Meyer, J., Moulis, J.-M., and Lutz, M. (1986) Resonance Raman spectroscopy of [2Fe-2X]²⁺ ($X = S, Se$) clusters in ferredoxins. *Biochim. Biophys. Acta* 873, 108–118.
 59. Atta, M., Lafferty, M. E., Johnson, M. K., Gaillard, J., and Meyer, J. (1998) Heterologous biosynthesis and characterization of the [2Fe-2S]-containing N-terminal domain of *Clostridium pasteurianum* hydrogenase. *Biochemistry* 37, 15974–15980.
 60. Yachandra, V. K., Hare, J., Gewirth, A., Czernuszewicz, R. S., Kimura, T., Holm, R. H., and Spiro, T. G. (1983) Resonance Raman spectra of spinach ferredoxin and adrenodoxin and of analogue complexes. *J. Am. Chem. Soc.* 105, 6462–6468.
 61. Xiao, Y., Wang, H., George, S. J., Smith, M. C., Adams, M. W. W., Francis, E., Jenney, J., Sturhahn, W., Alp, E. E., Zhao, J., Yoda, Y., Dey, A., Solomon, E. I., and Cramer, S. P. (2005) Normal mode analysis of *Pyrococcus furiosus* rubredoxin via nuclear resonant vibrational spectroscopy (NRVS) and resonance Raman spectroscopy. *J. Am. Chem. Soc.* 127, 14596–14606.
 62. Smulevich, G., and Spiro, T. (1995) Resonance Raman spectroscopy of metalloproteins. *Methods Enzymol.* 246, 416–460.
 63. Frey, R. A., Werder, R. D., and Günthard, H. H. (1970) Far infrared matrix spectra of iron chlorides Fe₂Cl₆, FeCl₃, Fe₂Cl₄, and FeCl₂. *J. Mol. Spectrosc.* 35, 260–284.
 64. Smith, M. C., Xiao, Y., Wang, H., George, S. J., Coucovani, D., Koutmos, M., Sturhahn, W., Alp, E. E., Zhao, J., and Cramer, S. P. (2005) Normal mode analysis of [FeCl₄][−] and [Fe₂S₂Cl₄]^{2−} via vibrational Mössbauer, Resonance Raman, and FT-IR Spectroscopy. *Inorg. Chem.* 44, 5562–5570.
 65. Shoji, M., Koizumi, K., Taniguchi, T., Kitagawa, Y., Yamanaka, S., Okumura, M., and Yamaguchi, K. (2007) Theory of chemical bonds in metalloenzymes III: full geometry optimization and vibration analysis of ferredoxin-type [2Fe-2S] cluster. *Int. J. Quantum Chem.* 107, 116–133.
 66. Spiro, T., and Czernuszewicz, R. S. (1995) Resonance Raman spectroscopy of metalloproteins. *Methods Enzymol.* 246, 4160460.
 67. Czernuszewicz, R. S., Macor, K. A., Johnson, M. K., Gewirth, A., and Spiro, T. G. (1987) Vibrational mode structure and symmetry in proteins and analogues containing Fe₄S₄ clusters: resonance Raman evidence for different degrees of distortion in HiPIP and ferredoxin. *J. Am. Chem. Soc.* 109, 7178–7187.
 68. Tinker: Software Tools for Molecular Design, <http://dasher.wustl.edu/tinker/>.
 69. Qiu, D., Dasgupta, S., III, and Spiro, T. G. (1998) Chromophore-in-protein modeling of the structures and resonance Raman spectra for type 1 copper proteins. *J. Am. Chem. Soc.* 120, 12791–12797.
 70. Saito, H., Imai, T., Wakita, K., Urushiyama, A., and Yagi, T. (1991) Resonance Raman active vibrations of rubredoxin. Normal coordinate analysis of a 423-atom model. *Bull. Chem. Soc. Jpn.* 64, 829–836.
 71. Cimei, T., Bizzarri, A. R., Cerullo, G., Silvestri, S. D., and Cannistraro, S. (2003) Excited state charge-transfer dynamics study of poplar plastocyanin by ultrafast pump-probe spectroscopy and molecular dynamics simulation. *Biophys. Chem.* 106, 221–231.
 72. Bizzarri, A. R., Paciaroni, A., Arcangeli, C., and Cannistraro, S. (2001) Low-frequency vibrational modes in proteins: a neutron scattering investigation. *Eur. J. Biophys.* 30, 443–449.
 73. Sage, J. T., Durbin, S. M., Sturhahn, W., Wharton, D. C., Champion, P. M., Hession, P., Sutter, J., and Alp, E. E. (2001) Long-range reactive dynamics in myoglobin. *Phys. Rev. Lett.* 86, 4966–4969.
 74. Doster, W., Cusack, S., and Petry, W. (1989) Dynamical transition of myoglobin revealed by inelastic neutron scattering. *Nature* 337, 754–756.
 75. Cusack, S., and Doster, W. (1990) Temperature dependence of the low frequency dynamics of myoglobin. Measurement of the vibrational frequency distribution by inelastic neutron scattering. *Biophys. J.* 58, 243–251.

76. Book, L. D., Arnett, D. C., Hu, H., and Scherer, N. F. (1998) Ultrafast pump-probe studies of excited-state charge-transfer dynamics in blue copper proteins. *J. Phys. Chem. A* **102**, 4350–4359.
77. Nakashima, S., Nagasawa, Y., Seike, K., Okada, T., Sato, M., and Kohzuma, T. (2000) Coherent dynamics in ultrafast charge-transfer reaction of plastocyanin. *Chem. Phys. Lett.* **331**, 396–402.
78. Iwasaki, T., Kounosu, A., Kolling, D. R. J., Crofts, A. R., Dikanov, S. A., Jin, A., Imai, T., and Urushiyama, A. (2004) Characterization of pH-dependent resonance raman transitions of Archaeal and bacterial Rieske [2Fe-2S] proteins. *J. Am. Chem. Soc.* **126**, 4788–4789.

BI701433M